2014

A straw tube tracking detector for the New Muon g-2 E989 experiment

Mary Elizabeth Shenk

ABSTRACT

A STRAW TUBE TRACKING DETECTOR FOR THE NEW MUON g-2 E989 EXPERIMENT

Mary Elizabeth Shenk, M.S.
Department of Physics
Northern Illinois University, 2014
Michael Eads, Director

The New Muon g-2 E989 Collaboration at Fermilab will measure the muon anomalous magnetic moment a_μ to a precision of 140 ppb, which represents a four-fold improvement in the experimental precision of the current value. Central to the E989 experiment is the muon storage ring magnet previously used by the E821 Collaboration at Brookhaven National Laboratory. The storage ring produces a highly precise magnet field. Muons will circulate the storage ring within a vacuum, and as the spin angular momentum of each muon precesses about the axis of the applied magnetic field, the muons will decay into positrons emitted preferentially along the instantaneous spin direction of the parent muon. Detectors will measure the energy and the number of high-energy positrons detected as a function of time, and the data will be analyzed to understand how much the muon's spin angular momentum is precessing. Specifically, the muon anomalous spin precession frequency ω_a and the average magnetic field $\langle B \rangle$ felt by the precession muons will be precisely measured by tracking detectors to extract the muon anomaly at the required precession. This paper focuses on the design, placement, and testing of the tracking detectors, and the development of the tracking detector simulation software.

NORTHERN ILLINOIS UNIVERSITY
DEKALB, ILLINOIS

DECEMBER 2014

A STRAW TUBE TRACKING DETECTOR FOR THE NEW MUON g-2 E989 EXPERIMENT

BY

MARY ELIZABETH SHENK

A THESIS SUBMITTED TO THE GRADUATE SCHOOL

IN PARTIAL FULFILLMENT OF THE REQUIREMENTS

FOR THE DEGREE

MASTER OF SCIENCE

DEPARTMENT OF PHYSICS

Thesis Director:
Michael Eads

ACKNOWLEDGEMENTS

I would like to thank my advisor and committee chair, Dr. Michael Eads. Without his guidance, support, and instruction this thesis would not have been possible. Dr. Eads always took time to answer my questions, and he generously funded me throughout my research.

I would also like to thank my committee members Dr. Michael Fortner and Dr. Jahred Adelman for taking time from their busy schedules to be on my thesis committee and to offer their insights regarding how to improve my thesis.

In addition, I would like to thank my colleagues, Dr. Leah Welty-Rieger, Ria Garg, Michael McEvoy, Octavio Escalante-Aguirre, Aaron Epps, and everyone else involved in New Muon g-2 E989 project, for their collaboration and hard work.

Finally, none of this work would have been possible without the continued support from my loved ones, Saroj, Gabriel, Mom, Dad, John, and Amy.

DEDICATION

To Saroj and Gabriel

TABLE OF CONTENTS

LIST OF TABLES

LIST OF FIGURES

Figure Page

Figure Page

PREFACE

My research concentrated on using computer simulation to help design and test a straw tube tracking detector for the New Muon g-2 E989 experiment at Fermilab. The simulation software used for the E989 experiment is described in chapter 5, and section 5.3 details the geometry acceptance study I performed to determine the optimal configuration of the tracker modules within the storage ring vacuum. In addition to my work on simulation, I also helped prepare the storage ring for reconstruction at Fermilab, as discussed in section 3.4, and I set up a cosmic ray test stand, discussed in chapter 2, at Northern Illinois University to test the muon flux rate at various locations so a suitable location could be chosen for possible future tests of the tracking detectors for the E989 experiment.

CHAPTER 1

INTRODUCTION

1.1 The Muon

In 1933, Paul Kunze observed an unknown particle in a Wilson cloud chamber exposed to cosmic rays. Although Kunze concluded the unknown particle ionized less than a proton and more than an electron, little was understood about the nature of the unknown particle, and it was not identified as a muon until 1936 when Carl Anderson and his first graduate student, Seth Neddermeyer, used a Wilson cloud chamber to measure the energy loss of cosmic ray particles interacting with dense materials like platinum (Kunze, and Anderson and Neddermeyer 263). Anderson and Neddermeyer determined the muon to have a rest mass between the rest masses of the electron and proton. The muon is now known to be a spin-½ fermion with a charge of $-e$. Hence, the muon is similar to an electron, except with a rest mass about 207 times as large (105.7 MeV/c^2) (Olive et al.). The muon's relatively large mass causes it to have less acceleration than electrons in a given electromagnetic field and, therefore, emit less bremsstrahlung radiation. Since the amount of energy loss due to bremsstrahlung is the main factor in how fast an electron or muon decelerates, muons are able to penetrate further into matter than electrons. The muon's weak interactions with matter, combined with the effects of time dilation experienced by a particle traveling at high speed,

also enable the muon to travel through the Earth's atmosphere and reach the Earth's surface. Not only do muons reach the Earth's surface at a rate of about one muon per square centimeter per minute (Olive et al.) as measured by a horizontal detector, but more muons are detected at sea level than other charged cosmic ray particles, and they are also able to penetrate several meters of solid matter. Muons have been detected underwater, deep in mines, and even inside an ancient Egyptian pyramid containing over 2,000,000 stones weighing about 2 tons each (Hutchings, ed. 18). Like the electron, the muon is a charged lepton. All leptons have a color charge of zero, so they do not undergo strong interactions. Instead, leptons interact with matter via the weak nuclear force, as well as the much weaker gravitational force. Due to its charge, the muon also interacts with matter via the electromagnetic force.

Most naturally occurring muons on Earth are created when cosmic rays interact with atomic nuclei in the upper atmosphere. Cosmic rays are primarily composed of protons, and many of these protons arrive from space at high energy. Once the protons reach Earth's atmosphere, they interact with the atomic nuclei of air molecules to form charged pions. Within a few meters, the charged pions decay into muons and the corresponding muon neutrinos. Negatively charged pions decay into negatively charged muons (μ^-), and positively charged pions decay into positively charged muons (μ^+), also called antimuons (Eisberg and Resnick 641). Muons typically lose 2 GeV of energy to ionization while passing through the atmosphere, and they reach the ground with a mean value of about 4 GeV of energy (Olive et al.). Unlike electrons, muons are unstable elementary particles and decay via the weak interaction according to the following two decay modes:

$$\mu^+ \rightarrow e^+ + \upsilon_e + \bar{\upsilon}_\mu \quad (1.1)$$
$$\mu^- \rightarrow e^- + \bar{\upsilon}_e + \upsilon_\mu. \quad (1.2)$$

Since the muon decays via the weak interaction, it has a longer mean lifetime in comparison to other unstable subatomic particles, and the lifetime has been measured to be τ_μ = (2.1969811 ± 0.0000022) × 10^{-6}s (Olive et al.). The muon's relatively long lifetime allows precision measurements to be made of the muon's mass, lifetime, and magnetic moment.

1.2 Muon Anomalous Magnetic Moment

According to Dirac's relativistic theory, a fermion's magnetic dipole moment, $\boldsymbol{\mu}$, is proportional to the spin angular momentum, **S**, by:

$$\boldsymbol{\mu} = g\left(\frac{Qe}{2m}\right)\mathbf{S} \quad (1.3)$$

where e is the elementary charge, m is the mass, g is the g-factor, and $Q = \pm 1$ depending on whether the fermion has a positive or negative charge. The classical magnetic dipole moment is naïvely given as $\boldsymbol{\mu} = \left(\frac{Qe}{2m}\right)\mathbf{S}$, so the g-factor in Dirac's theory indicates how much the magnetic dipole moment deviates from the classical expectation (Griffiths 284-285). The Dirac equation predicts the g-factor to be exactly 2 for particles like the muon and the electron, but relativistic quantum electrodynamics reveals small corrections to Dirac's value are necessary due to quantum loop effects. The corrections have been both calculated by theorists and measured by experimentalists. The true value of the g-factor is slightly larger than the Dirac value, and one-half the difference between the true value and Dirac's value is called the anomalous magnetic moment, a. For the muon, the anomalous magnetic moment can be precisely measured and, within the Standard Model framework, precisely predicted.

Thus, comparison between experiment and theory tests the completeness of the Standard Model at the quantum loop level (Beringer et al. 1).

The Standard Model theoretical value for the muon anomalous magnetic moment contains three parts:

$$a_\mu^{\mathrm{SM}} = a_\mu^{\mathrm{QED}} + a_\mu^{\mathrm{EW}} + a_\mu^{\mathrm{Had}}. \tag{1.4}$$

The quantum electrodynamics (QED) part is by far the largest component of the muon anomalous magnetic moment and includes contributions from photon and lepton loops. The electroweak (EW) part is the smallest component of the muon anomalous magnetic moment and includes contributions from the loops of heavy $W^{\pm}$, Z, and Higgs particles. The hadron (Had) part includes contributions from quark and gluon loops. The QED part is well understood, and the first order correction is the $\alpha/2\pi$ Schwinger contribution (Schwinger 790). The QED and EW parts can be precisely calculated from the Standard Model theory. The QED contribution has been calculated through five loops to be $a_\mu^{\mathrm{QED}} = 116\,584\,718\,951\,(80) \times 10^{-14}$ (Aoyama et al. 1), and the EW contribution has been calculated through two loops to be $a_\mu^{\mathrm{EW}} = 153.6\,(1.0) \times 10^{-11}$ (Gnendiger et al.), but the hadron contribution cannot be calculated from first principles alone and presents the main theoretical uncertainty in the muon anomalous magnetic moment. The uncertainty primarily comes from the $O(\alpha^2)$ hadronic vacuum-polarization term, where α is the fine-structure constant. Currently, most accurate evaluations of the hadronic vacuum-polarization term rely on experimental information. The theoretical value of the muon anomalous magnetic moment has been calculated within the Standard Model to be $a_\mu^{\mathrm{SM}} = 116\,591\,840\,(59) \times 10^{-11}$

(Aoyama et al. 4), though improvements in the value are expected to be published in the relatively near future.

The equation for the muon magnetic dipole moment can be separated into two terms (Roberts et al. 36):

$$\mu = \frac{e\hbar}{2m_\mu} + a_\mu \frac{e\hbar}{2m_\mu} = \left(1 + a_\mu\right)\frac{e\hbar}{2m_\mu} \tag{1.5}$$

where $a_\mu = \frac{g-2}{2}$ is the muon anomalous magnetic moment and m_μ is the muon mass. The first term, $\frac{e\hbar}{2m_\mu}$, comes from Dirac's theory, and the second term, $a_\mu \frac{e\hbar}{2m_\mu}$, arises from the muon anomaly. The most recent measurement of the muon anomalous magnetic moment was performed by the Muon g-2 E821 Collaboration at Brookhaven National Laboratory (BNL). In 2006, the E821 Collaboration published their final result as (Bennett et al.):

$$a_\mu^{\mathrm{E821}} = 11659208.0(5.4)_{\mathrm{stat}}(3.3)_{\mathrm{syst}}(6.3)_{\mathrm{tot}} \times 10^{-10}(\pm 0.54\mathrm{ppm}), \tag{1.6}$$

where the statistical, systematic, and total uncertainties are given, respectively. The combined uncertainty of 0.54 ppm represents a 14-fold improvement in comparison with previous measurements done at CERN (Bailey et al.). The value of the muon anomalous magnetic moment measured by the E821 Collaboration differs from the value predicted by the Standard Model by 3.3 to 3.6 standard deviations, depending on which evaluation of the lowest-order hadronic contribution from the Standard Model is used (Roberts et al. 6). As a result, theorists and experimentalists have studied the hadronic contributions in an attempt to account for the discrepancy.

The muon anomalous magnetic moment is more sensitive than the electron anomalous magnetic moment to contributions from heavy virtual particles, so the muon anomaly can be

measured with less precession than in the case of the electron and still be sensitive to masses in the several hundred GeV region. The several hundred GeV region includes contributions from the *W* and *Z* bosons, as well as the potential for contributions from currently undiscovered particles, such as the possible supersymmetric partners of the electroweak gauge bosons. A more precise measurement of the muon anomalous magnetic moment could also deepen mankind's understanding of physics concepts and interactions by opening the door to new physics beyond the Standard Model, or by placing constraints on current and future physics models.

1.3 Measuring the Muon Anomalous Magnetic Moment

Experiments involving the muon magnetic dipole moment usually inject a beam of polarized muons into a precisely measured magnetic field and measure the anomalous spin precession frequency, ω_a, which is the rate the muon polarization (or spin) turns relative to the momentum. A magnetic field can be used to bend a muon beam into a circle with a prescribed radius for orbiting a storage ring. In a storage ring exposed to a uniform magnetic field, muons circulate the ring at the cyclotron frequency, ω_C, and the muon spin precesses about the magnetic field at the Larmor (or spin) frequency, ω_S. The anomalous spin precession frequency is the difference between the Larmor and cyclotron frequencies: $\omega_a = \omega_S - \omega_C$. The muon cyclotron and spin frequencies in the presence of a uniform applied magnetic field, but no other external fields, are given by (Roberts et al. 38):

$$\omega_C = -\frac{Qe}{m_\mu \gamma} B \tag{1.7}$$

$$\omega_S = -g\frac{Qe}{2m_\mu}B - (1-\gamma)\frac{Qe}{m_\mu\gamma}B = -\frac{Qe}{m_\mu}B\left(\frac{1}{2}g + \frac{1}{\gamma} - 1\right) \tag{1.8}$$

where $e > 0$, $Q = \pm 1$, B is the applied magnetic field, and $\gamma = \frac{1}{\sqrt{1-v^2/c^2}}$ is the Lorentz factor. Thus, the anomalous spin precession frequency is given by:

$$\omega_a = \omega_S - \omega_C = -\left(\frac{g-2}{2}\right)\frac{Qe}{m_\mu}B = -a_\mu\frac{Qe}{m_\mu}B. \tag{1.9}$$

As shown above, ω_a depends on the muon anomaly, a_μ, rather than the full dipole moment, μ, and ω_a depends linearly on the applied magnetic field, B.

In the third iteration of a series of muon g-2 experiments performed at CERN, it was discovered that an electrostatic quadrupole field can be used to vertically focus a muon beam (Bailey et al.). An electric field, as opposed to the more common method of using a series of quadrupole magnets, is preferred for beam focusing because any additional magnetic field would interrupt the constant, well-measured magnetic field necessary for measuring a_μ. In the presence of both a magnetic and an electric field, equation (1.9) is modified to give:

$$\boldsymbol{\omega}_a = -\frac{Qe}{m_\mu}\left[a_\mu\boldsymbol{B} - \left(a_\mu - \left(\frac{m_\mu c}{p}\right)^2\right)(\boldsymbol{\beta}\times\boldsymbol{E})/c\right] \tag{1.10}$$

where $\boldsymbol{\beta}$ is the velocity of the muon as it travels around the storage ring and p is the muon momentum. If, however, the storage ring is operated at the magic momentum, $p_{magic} = m_\mu/\sqrt{a_\mu} \cong 3.094\,\mathrm{GeV}/c$, then $a_\mu - \left(\frac{m_\mu c}{p}\right)^2 = 0$ and the electric field contribution cancels to first order. At the magic momentum, equation (1.10) essentially reduces to equation (1.9). Small corrections to second order, though, must be added to the observed anomalous spin precession frequency to obtain the measured muon anomaly because in reality the velocity $\boldsymbol{\beta}$ is not completely transverse to the magnetic field B, and not all the muons have a momentum

equal to the magic momentum (Farley and Picasso 479). To make the corrections, the vertical betatron motion must be included, and the muons must be given a range of momenta not quite at the magic momentum. Similar to the E821 experiment, these will be the only two corrections made to the E989 data for ω_a (Roberts et al. 96).

In an idealized experiment, the muon anomaly a_μ would be obtained from a measurement of ω_a via the relationship

$$\omega_a = -a_\mu \frac{Qe}{m_\mu} B. \tag{1.11}$$

Using equation (1.11), the applied magnetic flux density $|\boldsymbol{B}|$ and the muon charge to mass ratio e/m_μ would need to be precisely measured. For muons, the value of $|\boldsymbol{B}|$ can be determined from proton nuclear magnetic resonance (NMR) measurements (Mohr, Taylor, and Newell 1549), but due to uncertainties in the muon charge to mass ratio, a_μ would have an uncertainty of 41 ppb (Roberts et al. 431). Instead, higher precision can be achieved by obtaining a_μ from

$$a_\mu = \frac{\omega_a/\omega_p}{\mu_{\mu^+}/\mu_p - \omega_a/\omega_p} \tag{1.12}$$

where ω_a is the anomalous spin precession frequency, ω_p is the free proton precession frequency, and μ_{μ^+}/μ_p is the muon-to-proton magnetic moment ratio. The E1054 LAMPF measurement of Zeeman ground state hyperfine transitions in muonium (the μ^+e^- atom) found $\lambda_+ = \mu_{\mu^+}/\mu_p = 3.183\,345\,24(37)$ with an uncertainty of 120 ppb (Liu et al. 711). Note, ω_p must be in the same flux density $|\boldsymbol{B}|$ as seen by the muons. The value of ω_p is also weighted by the muon distribution in the storage ring, as well as averaged over the running time weighed by the number of stored muons. Using a spherical water probe to get an

absolute calibration of the magnetic field relative to the Larmor frequency of the free proton allows the magnetic field to be expressed in terms of the Larmor frequency of a free proton, ω_p, via the relationship $\omega_p = \gamma_p|\boldsymbol{B}|$, where $\gamma_p$is the free proton gyromagnetic ratio. The value of ω_p can then be combined with the average value of ω_a to obtain the muon anomaly a_μ from a modified version of equation (1.12):

$$a_\mu = \frac{\omega_a/\omega_p}{\mu_{\mu^+}/\mu_p - \omega_a/\omega_p} = \frac{\mathcal{R}}{\lambda_+ - \mathcal{R}} \tag{1.13}$$

where $\mathcal{R} = \omega_a/\omega_p$ and $\lambda_+ = \mu_{\mu^+}/\mu_p$. If λ_+ is used to determine a_{μ^-}, rather than a_{μ^+}, then CPT invariance must be assumed, meaning $a_{\mu^+} = a_{\mu^-}$ and $\lambda_+ = \lambda_-$. Therefore, a comparison of $\mathcal{R}_{\mu^+}$ with $\mathcal{R}_{\mu^-}$ is a CPT test. The E821 Collaboration at BNL measured $\mathcal{R}_{\mu^+}$ and $\mathcal{R}_{\mu^-}$ and found the difference to be (Roberts et al. 85):

$$\Delta\mathcal{R} = \mathcal{R}_{\mu^-} - \mathcal{R}_{\mu^+} = (3.6 \pm 3.7) \times 10^{-9}. \tag{1.14}$$

1.4 Motivation for the Muon g-2 E989 Experiment

The primary goal of the New Muon g-2 E989 Collaboration at Fermilab is to measure the muon anomalous magnetic moment, a_μ, with a four-fold improvement in the experimental precision of the current value (Roberts et al. 22). The error will be reduced to 140 ppb, which is comparable to the 400 ppb error on the value predicted by the Standard Model (Roberts et al. 22). In the most recent measurement of a_μ, the E821 Collaboration found the experimental value to differ unexpectedly from the Standard Model prediction by more than three standard deviations. This discrepancy between measurement and theory could mean the Standard Model needs to be extended to include, for example, supersymmetry, extra dimensions, or the

postulated dark photon. However, the greater than 3σ difference found by E821 was statistics limited and does not meet the 5σ threshold for claiming a discovery, so a more precise measurement is needed to rule out statistical fluctuations and confirm the discrepancy between experiment and theory found by E821. To obtain the necessary precision, the E989 experiment will observe the muon spin precession with more than 20 times the statistics of the E821 experiment, while controlling systematics to the 100 ppb level. The new g-2 experiment will take advantage of the Fermilab accelerator complex to produce an intense beam with more muons than can be produced by any other accelerator in the United States, and the individual project components will either be newly constructed, or upgraded and modified, to meet higher precision demands. Ultimately, a more precise measurement of a_μ offers a unique way to search for new physics and gain a deeper understanding of the universe at the most fundamental level. Even if the E989 measurement agrees with the value predicted by the Standard Model, the new measurement could place stricter limits on current and future theories. If, however, the E989 measurement differs from the theoretical value, the higher precision could point to new forces and new particles. Greater precision is also expected to give a direct measurement of the coupling constants of the possible new particles causing the measured a_μ to deviate from the Standard Model value. Furthermore, the outcome of the E989 experiment will help inform choices for future projects in high energy and particle physics, no matter what value is measured for a_μ.

1.5 Overview of the Muon g-2 E989 Experiment

To measure the muon anomaly, a_μ, precise measurements must be made of the anomalous spin precession frequency, ω_a, and the magnetic field, B, averaged over the muon distribution. The free proton precession frequency, ω_p, will also be measured for use in the relationship given by equation (1.13). Making the measurements, though, will involve several steps.

First, a beam of polarized muons is obtained by producing a pulsed proton beam in the Fermilab accelerator complex. A bunched proton beam from the 8GeV Booster will then be smashed into a fixed pion production target. Shortly thereafter, the charged pions produced in the collision undergo a weak decay to form muons/antimuons and muon neutrinos/antineutrinos, according to the schemes $\pi^- \rightarrow \mu^- + \bar{\upsilon}_\mu$ and $\pi^+ \rightarrow \mu^+ + \upsilon_\mu$. The daughter muons will have a spin pointing along the direction of the parent pion. Magnets will steer the pions and muons to the 14-meter-diameter Muon Delivery Ring (formerly the antiproton debuncher ring). Virtually all the remaining pions will decay into muons while traveling around the delivery ring. To get polarized muons, either the highest-energy muons are selected to create a "forward beam," or the lowest-energy muons are selected to create a "backward beam," where forward and backward refer to the direction of decay in the pion rest frame. In particular, the "forward" decay muons are highly polarized and have the highest laboratory momenta with a direction nearly parallel to the pion laboratory momentum (Roberts et al. 79), so they will be used for the first run of the E989 experiment. Also, negative muons tend to be captured in matter more often than positive muons, so positive

muons are easier to work with. Negative muons, though, may be used in a second run of the E989 experiment.

Next, the polarized muons are collected, transferred through the inflector magnet, and injected into the same 50-foot-diameter muon storage ring used for the E821 experiment at Brookhaven. Initially, muons enter the storage ring on the injection orbit, slightly offset from the storage ring orbit. Electromagnetic kicker modules put the muon beam onto the storage ring orbit. While circulating the storage ring, the positive muons continually decay to positrons, electron neutrinos, and muon antineutrinos, as shown in equation (1.1). The negative muons decay to electrons, electron antineutrinos, and muon neutrinos, as shown in equation 1.2. The neutrinos and antineutrinos are not detected, but the electrons/positrons can be measured, and they carry information about the spin of the parent muon. Due to the ($V - A$) weak decay of the muon, the highest energy positrons coming from the μ^+ decay will be emitted parallel to the muon spin in the muon rest frame, and the highest energy positrons coming from the μ^- will be emitted anti-parallel to the muon spin. Finally, the electron/positron energy and the number of high energy electrons/positrons detected as a function of time, among other measurements, will be measured by various detectors throughout the storage ring. For the first run of the E989 experiment, data taking will begin in 2016 and continue for two years. In the coming years, the data will be analyzed to extract the muon anomaly a_μ. The E989 experiment will measure a_{μ^+} during the first run, and a_{μ^-} may be measured in a second run. Theoretically, a_{μ^+} should equal a_{μ^-}, but measuring both provides a way to perform a CPT test, as mentioned above in the discussion of equation (1.13). Since the values measured for a_{μ^+} and a_{μ^-} in the E821 experiment were statistically

consistent, the E821 Collaboration averaged the two values to produce their final experimental value for a_μ.

CHAPTER 2

COSMIC RAY TEST STAND

2.1 Introduction and Motivation for Cosmic Ray Tests

Earth is continually bombarded by high-energy particles from space, most of which are protons (hydrogen nuclei). The protons quickly decay into a cascade of decay products, but since Earth's atmosphere is equivalent to ten nuclear interaction lengths (Melissinos and Napolitano 399), the strongly interacting decay products are absorbed, leaving muons to be the most numerous charged particle found at sea level. Therefore, preliminary research and experimentation with the straw tube tracking detectors for the E989 experiment can make economic use of cosmic muons, as opposed to muons generated by Fermilab's accelerator complex. The goal of the cosmic ray tests was to measure the incoming count rate of muons at various locations in Faraday and Faraday West at Northern Illinois University (NIU), and make a comparison to the muon count rate measured outdoors. A high flux of charged particles, such as cosmic muons, is desired when experimenting with the straw tube detectors. Thus, the results from the cosmic ray tests can be used to choose the best indoor location for future straw tube research to be performed at NIU.

To measure the incoming rate of cosmic muons at a particular location, a cosmic ray detector consisting of scintillator paddles, each attached to a photomultiplier tube, can be

used. Scintillator paddles work by converting the kinetic energy of incident muons, or other charged particles, to photons. The photons excite nearby electrons, and the excited electrons emit additional photons in the form of light when returning to the ground state. The photomultiplier tubes then convert each small flash of light into a current. The current is multiplied into a large electrical signal, and the signal is sent to a coincidence unit to be counted.

The scintillator paddles used in the cosmic ray tests are leftover from the DZero Run II upgrade (Abazov et al. 372). The paddles are made from an acrylic-based plastic with the ability to produce a light flash when struck by a charged particle. Each paddle is fully enclosed to exclude stray light so only cosmic rays were detected. Figure 2.1 shows a schematic of a photomultiplier tube coupled to a scintillator (not to scale). A charged particle enters the scintillator from the left and is converted to a photon. The photocathode at the front of the tube is a photoelectric surface with a low enough work function for an electron to be released when a photon from the scintillator paddle strikes the photoelectric surface. The electrode focuses electrons from the photocathode into a beam, and aims the beam at the current multiplier. The multiplier is a series of dynodes, or electrodes, maintained at successively higher voltages. The increasing potential differences accelerate the electron beam in steps, giving the electrons higher kinetic energy at each dynode. Every time the kinetic energy of the electron beam is increased and the beam strikes another dynode, more electrons are released. Thus, the multiplier increases the number of electrons in the beam, and the number of electrons striking the last dynode may be 10^6 or more (Giancoli 1080), enabling individual charged particles incident on the scintillator to be detected. After passing through

the multiplier, the final number of electrons is collected as a current at the anode. The output signal at the anode is a measurable pulse for each photon detected at the photocathode, and the current is sent via electric wires to be counted.

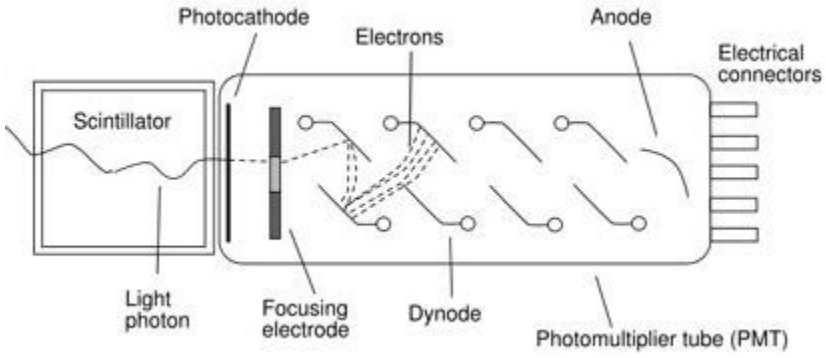

Figure 2.1: Schematic diagram of a scintillation detector comprising a scintillation material coupled to a photomultiplier tube. A charged particle enters from the left. (Image courtesy of http://web.stanford.edu/group/scintillators/scintillators.html).

2.2 Procedure

The apparatus for the cosmic ray tests consisted of three scintillator paddles (approximately three feet by one foot in area) with photomultiplier tubes (numbered 005, 014, and 028), a quad discriminator, a dual channel scaler, a coincidence unit, an NIM power chassis, a high voltage divider, and a high voltage DC power supply. The scintillators were designed to be operated at voltages up to 2000 V, so the first step in the cosmic ray tests was to determine the optimal operating voltage for each scintillator by measuring the muon counts per minute as a function of voltage. All three scintillators were tested in the southwest corner of Faraday101 with voltages ranging from 1400 V to 2000 V. Plots of the data, shown below,

were expected to show the counts per minute go up as the voltage was increased until a plateau was reached where increasing the voltage did not significantly affect the count rate. The operating voltage was chosen to be the highest voltage located just before the plateau on the graph so as to obtain the highest count rate with a minimum level of noise. Based on the results of the muon count rate measurements and the voltage plateau plots for the scintillator paddles, paddle 028 was operated at 2000 V, paddle 014 was operated at 1840 V, and paddle 005 was operated at 1800 V.

For the cosmic ray tests, muon count rates were measured at eight locations: Faraday 101 in both the center of the room and in the southwest corner, Faraday 215, Faraday West 226, Faraday West 230, the fourth floor of Faraday West at both the north and south ends of the central corridor, and outdoors at the fountain behind Davis Hall. The muon count rates in Faraday 101 were of particular interest because Faraday 101 is the laboratory where NIU research and experimentation with the straw tube detectors was to take place. Measurements were taken using one, two, and three scintillator paddles in a horizontal position and stacked directly over one another, except for one set of data taken in Faraday West 230 where the paddles were angled at approximately 45° toward the window. At least three trials were conducted for each measurement, and the data was averaged. Each trial was ten minutes long for the triples, five minutes long for the doubles, and one minute long for the singles. The count rate decreases as the muon is required to go through more paddles, so longer times for the doubles and triples were necessary to reduce error caused by insufficient statistics.

2.3 Results and Conclusions

Figures 2.2, 2.3, and 2.4 show the voltage plateau plots for scintillators 005, 014, and 028, respectively. As discussed in section 2.2, the operating voltage was chosen to be the voltage just before a plateau in the muon count rate was reached. Scintillator 005 appeared to reach a plateau at about 1800 V, scintillator 014 appeared to reach a plateau at about 1840 V, and scintillator 028 appeared to reach a plateau at about 2000 V, which is the maximum allowable operating voltage. However, after analyzing the data from the cosmic ray tests, scintillator 028 seemed to have been operated at too high a voltage because its muon count rates were several times higher than the count rates for scintillators 005 and 014. For all three scintillators, the muon count rate reached a plateau at slightly less than one count per minute.

Table 2.1 summarizes the average muon count rates for the eight locations tested using different combinations of the scintillator paddles. As shown, the count rates were highest for the measurements taken outdoors, and they were the next highest in Faraday 215 (the physics teaching assistant office) and at the north end of the fourth floor central corridor in Faraday West. Both Faraday 215 and the fourth floor of Faraday West have windows. Plus, the fourth floor of Faraday West has large skylights, and is at a higher altitude and has less building material for muons to traverse in comparison to the other indoor locations tested. The count rates were also high for the singles using paddle 028, but this is most likely due to noise caused by operating the paddle at too high a voltage. Some of the lowest count rates were measured for the trial where the scintillators were placed in an angled position, as opposed to a horizontal position. Although the paddles were angled toward a window, muons traveling

vertically through the atmosphere are more likely to have enough kinetic energy to reach the Earth's surface because muons traveling at an angle pass through more atmosphere and loose more energy to ionization. For example, a muon traveling at a 45° angle to the vertical travels through at least 1.4 times more atmosphere than a muon traveling vertically, and a muon traveling at an 85° angle travels through 11 times more atmosphere (Harpell et al. 3). Therefore, muons traveling at an angle are more likely to decay before reaching the scintillators. Since a larger percentage of the muons with enough kinetic energy to reach the paddles are traveling vertically, the horizontal paddles have more active area for the muons to strike.

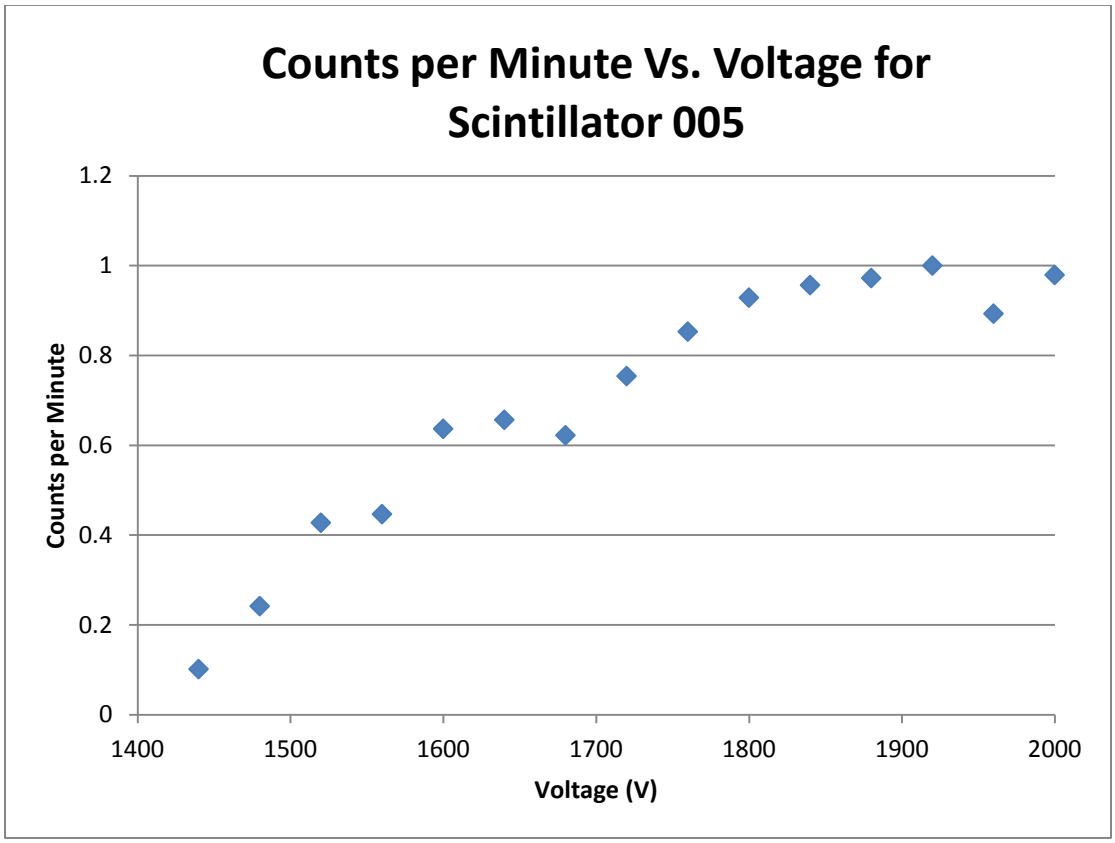

Figure 2.2: Muon count rate as a function of voltage for scintillator 005. The vertical scale has been normalized so the maximum number of counts per minute is at unity.

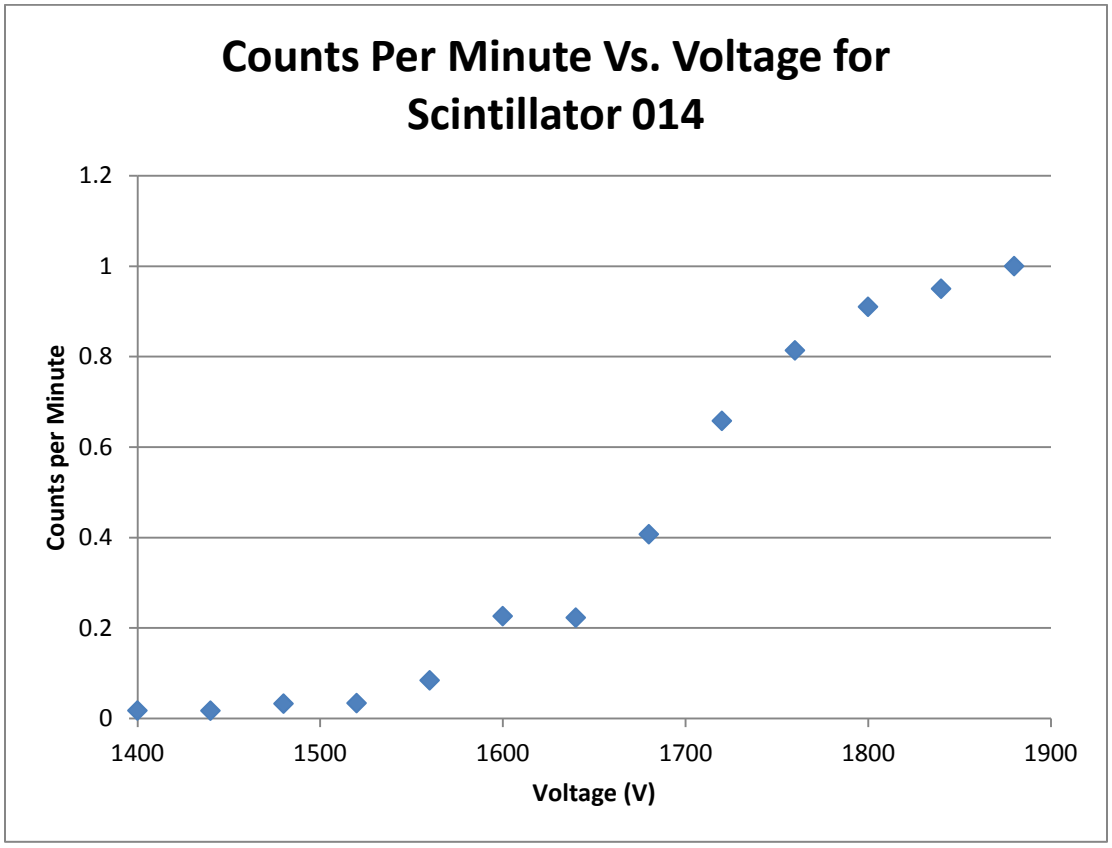

Figure 2.3: Muon count rate as a function of voltage for scintillator 014. The vertical scale has been normalized so the maximum number of counts per minute is at unity.

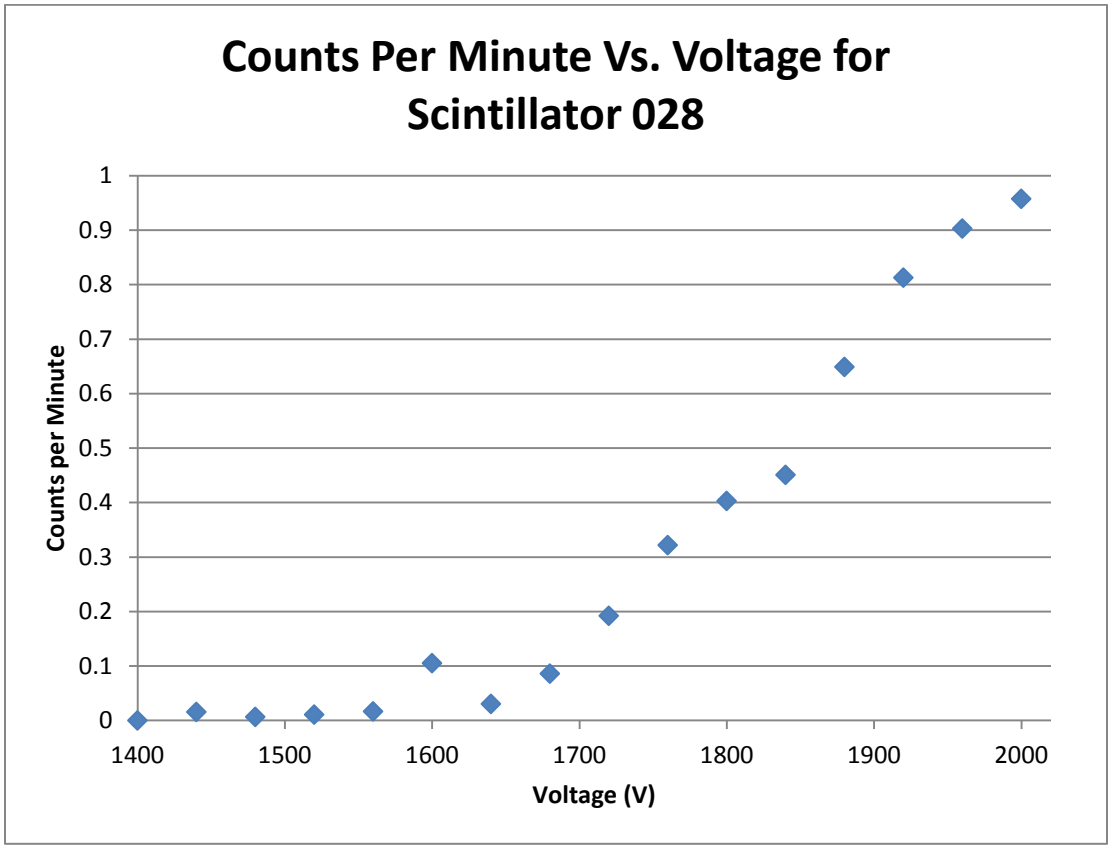

Figure 2.4: Muon count rate as a function of voltage for scintillator 028. The vertical scale has been normalized so the maximum number of counts per minute is at unity.

Table 2.1: Average Muon Counts per Minute for Various Locations in Faraday (FR), Faraday West (FW), and Outside.

	Average counts per min ($\bar{N}$/min)								
Scintillator, bottom scintillator listed first	Center of FR 101	SW corner of FR 101	4th. Floor FW, north end	4th. Floor FW, south end	Dr. Blazey's office, FW 230 (stacked setup)	Dr. Blazey's office, FW 230 (angled setup)	NICADD office, FW 226	TA office, FR 215	Outside
028/014/005	352 ±10.3	400 ±13	540 ±12.7	476 ±11.9	476 ±12	329 ±9.9	416.7 ±11.2	544.2 ±12.8	645.5 ±13.9
014/005	516 ±12.4	480 ±17	675 ±20.	601 ±19.1	574 ±18.6	462 ±16.7	544.3 ±18.1	653.9 ±19.8	816.2 ±22.1
028/014	588 ±18.8	443 ±16	570 ±18.5	503 ±17.4	484 ±17.0	482 ±17.0	511 ±18	618.7 ±19.2	3751 ±21
028/005	1180 ±27	1025 ±25	1354 ±29	1288 ±28	1094 ±26	1049 ±25	1050 ±25	1306 ±28	7839 ±31
028	7903 ±154	4434 ±115	28,648 ±293	12,120. ±191			17,268 ±228	18,897 ±238	229,140 ±829
014	2146 ±80.	1066 ±57	2729 ±90.	3624 ±104			1472 ±66	1338 ±63	2370 ±84
005	3904 ±108	2723 ±128	3283 ±99	3237 ±99			3277 ±99	3643 ±105	4197 ±112

The count rates were also low in Faraday 101, presumably because Faraday 101 is located in a windowless basement, surrounded by dirt, cement, and other material. As the muons traverse the material above Faraday 101, they interact with the atoms in the material and loose energy, so fewer muons reach the scintillation paddles. As a result, Faraday 101 does not appear to be the ideal location for using cosmic ray muons to conduct preliminary testing of the straw tube detectors. Recently, though, the E989 collaborators at the University of Liverpool in the United Kingdom received a grant to construct and build the straw tube tracking detectors, so the decision was made for most of the assembly and testing to take

place in the United Kingdom, instead of at NIU. Therefore, the rate muons enter the laboratory in Faraday 101 is now less of a concern.

CHAPTER 3

THE MUON STORAGE RING MAGNET

3.1 Introduction

Central to the g-2 E989 experiment at Fermilab is the fourteen-meter-diameter muon storage ring magnet previously used in the E821 experiment at Brookhaven. The storage ring is designed to contain muons within a constant, uniform magnetic field until the muons decay via the weak interaction. Muons with aligned spins will be injected into the storage ring, and as the muons orbit the storage region vacuum, their magnetic dipole moments will experience a torque and tend to rotate to align with the axis of the applied magnetic field. Full alignment, though, will be prevented by the muons' intrinsic spin angular momenta. Instead, the spin angular momentum of each muon will precess about the axis of the applied magnetic field. Depending on whether positive or negative muons are being used, the muons will decay into either positrons or electrons and the corresponding neutrinos and antineutrinos. The positrons/electrons are emitted preferentially along the instantaneous spin direction of the parent muon (Cox 2-3). Detectors inside the storage ring vacuum will measure the energy and the number of high-energy positrons/electrons detected as a function of time, and the data will be analyzed to understand how much the muon's spin angular momentum is precessing. In particular, the rate the muon polarization turns relative to the momentum, ω_a, and the average magnetic field felt by the precessing muons, $\langle B \rangle$, must be measured precisely so the muon

anomalous magnetic moment, a_μ, can be extracted at a precision of 140 ppb. Ultimately, the design, construction, shimming, and operation of the storage ring is indispensable to obtaining the muon anomalous magnetic moment at the required precision.

3.2 Storage Ring Design

The storage ring is constructed as a single continuous superferric magnet energized by three superconducting coils. It is designed to maintain a homogenous magnetic field $B = 1.451\,\mathrm{T}$ so muons traveling at the magic momentum $\left(p_{magic} = 3.094\,\mathrm{GeV}/c\right)$ will be constrained to move in a circle with a central orbit radius of 7.112 meters (Danby, et al. 153). The storage ring was built for the E821 experiment and, in designing the ring, two options were available regarding the experimental method: 1) both the muon trajectories and the magnetic field at each point would need to be known at the tens of parts per billion level, or 2) the muon trajectories would need to be reasonably understood, and the magnetic field would need to be as uniform as possible and precisely measured. Since the muon distribution cannot be measured with high precision, the goal in the E821 experiment was to produce a uniform magnetic field, both azimuthally and across the storage region cross section. Uniformity along the azimuth also improves NMR measurements of the magnetic field and simplifies analysis of the average magnetic field seen by the muons. Thus, strict requirements for a uniform, well-measured magnetic field was driving factor in design of the storage ring, and a shimming kit further reduced variations in the magnetic field caused by mechanical assembly of the magnet.

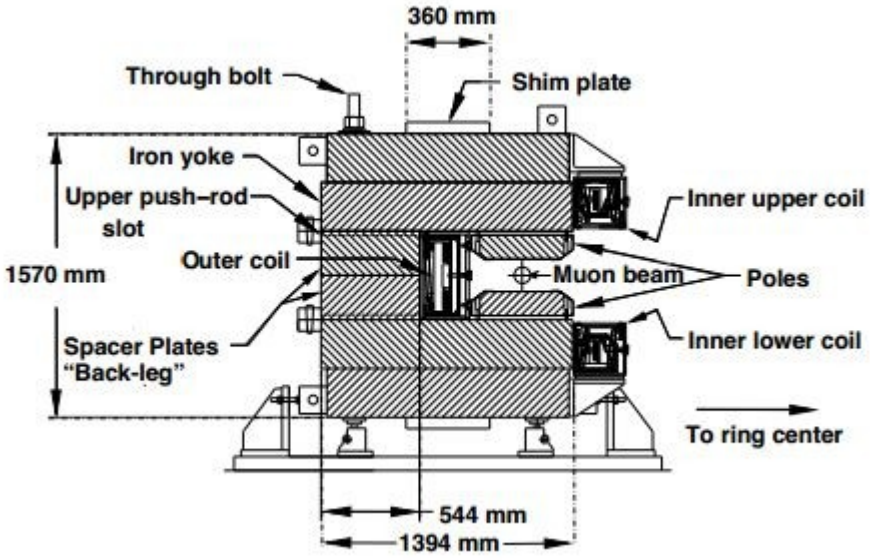

Figure 3.1: Cross-section of the storage ring showing the C-shaped magnet yoke and the three superconducting coils. (Image courtesy of B. Lee Roberts, FNAL).

The storage ring includes the fourteen-meter-diameter C-shaped iron yoke, the pole pieces, and three superconducting coils. The pole pieces help make the magnetic field more uniform, and the superconducting coils energize the magnet. Figure 3.1 shows a cross-section of the storage ring. The magnet yoke is built from twelve 30° iron sectors, and the superconducting coils are made of titanium-niobium filaments in a copper matrix and surrounded by a pure aluminum stabilizer. Conventional AISI 1006 iron (usually 0.07% carbon content) is used for the magnet yoke, whereas the highest quality iron (0.004% carbon content) is reserved for the pole pieces. Wedge-shaped air gaps between the yoke and the poles isolate the poles from non-uniformities in the yoke iron, so the pole pieces contribute more than the magnet yoke to magnetic field aberrations. Therefore, ferritic inclusions, air

bubbles, and other impurities and imperfections were minimized during fabrication of the pole pieces.

Each of the 30° yoke sectors has an upper and lower yoke separated by a spacer plate, as depicted in Figure 3.1. The magnet is C-shaped so the muon decay products can be observed and measured inside the storage ring. The opening of the "C" faces the center of the ring, and the muon storage region inside the "C" has a 9 cm diameter. The spacer plate is split horizontally at the midplane so beam pipes, transfer lines, and electrical connections to the outer coil cryostat can be installed after the lower half of the storage ring is placed, but before the upper half is placed. The yokes and spacer plates in each 30° sector are vertically fastened together with eight high-strength steel bolts (super bolts), 5 cm in diameter. The assembled sectors are each 1.57 m tall with a mass of about 57,000 kg, giving the total magnet a mass of about 680,000 kg (Roberts, et al. 282). Each 30° sector has four radial projections (ears) near the bottom of the yoke. To achieve azimuthal continuity in the yoke magnet, the sectors are joined together in a circle with bolts going through the ears.

Due to the cost of purchasing iron to build the storage ring, the total flux and the yoke cross section were minimized, leading to a narrow pole design. The narrow poles, however, work against producing a uniform magnetic field over the storage region aperture, so a tapered pole shape was chosen to reduce variations in the iron permeability and the magnetic field throughout the pole (Danby, et al. 154). Figure 3.2 shows a cross-sectional view of the poles lining the magnet gap. The pole pieces are mounted to the yoke plates with steel bolts. The pole pieces were constructed in 10° azimuthal sections, so three poles are attached to the bottom face of each top yoke, and three poles are attached to the top face of each bottom

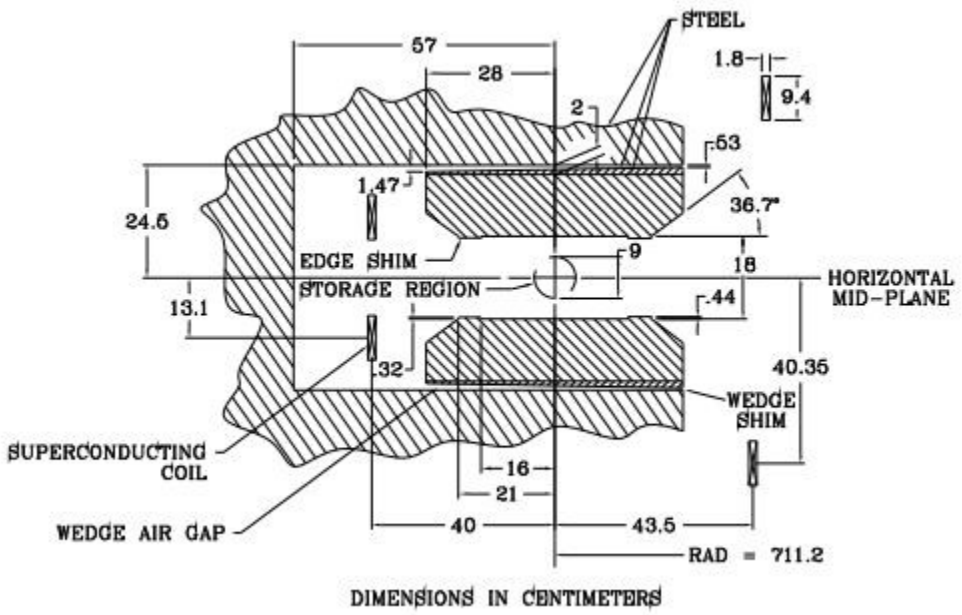

Figure 3.2: Cross-section of magnet gap showing the storage region, the wedge shims, and the poles. (Image courtesy of B. Lee Roberts, FNAL).

yoke. The middle pole in each group of three is interlocking, with an angle of 7° with respect to the radial direction. Kapton shims, 80 μm thick, between the poles help position each pole to the correct azimuth and keep the poles electrically isolated from one another. Large eddy currents around the circumference of storage ring would result if the poles were electrically connected, so the kapton shims are important to keep the eddy currents small and reproducible during field ramping and energy extraction.

For the entire storage ring, a total of 72 pole pieces line the top and bottom of the magnet gap. Each pole surface has a flatness tolerance of 25 μm, meaning the upper and lower pole surfaces are parallel with a 50 μm tolerance (Roberts, et al. 283). Non-parallel surfaces introduce a large quadrupole moment, and each term in a multipole expansion of the average magnetic field $\langle B \rangle$ seen by the muons reduces the precision. Therefore, the goal is for only the

leading term to be large, which makes just the first few multipoles important in determining $\langle B \rangle$. The E821 experiment used a circular beam aperture and a uniform dipole magnetic field to minimize non-leading terms, and the E989 experiment plans to do the same.

As part of the storage ring design, 2-cm wide air gaps were left between the yokes and pole pieces for three reasons: 1) to decouple the yoke iron from the poles so the magnetic field quality is minimally affected by yoke imperfections, 2) to allow space for each pole's flat dipole correction coil so the dipole field in the azimuth can be adjusted, and 3) to allow space for iron wedges to be inserted so the magnetic field can be fine-tuned to compensate for the intrinsic quadrupole moment induced by the C-shaped magnet. For the iron wedges, the slope of the wedge affects the quadrupole moment, and the radial position of the wedge affects the dipole moment by changing the amount of material in the shimming gap. The wedges are 0.5 cm thick at the outer radius of the storage ring and 1.65 cm thick at the inner radius. The wedges are 9.86 cm wide in the azimuthal direction and 53 cm long in the storage ring's radial direction (Danby et al. 151). When the main coil current is ramped, the thick end of the wedge attracts more magnetic field lines, leading to a torque on the wedge. To keep the wedges from deflecting vertically, clamps were made from aluminum sheets taped together to form an "anti-wedge" shape, and the clamps were inserted beside the wedges. The wedges are part of the passive, or mechanical, shimming of the storage ring that will be performed during assembly of the storage ring and will remain fixed throughout the running period. Active, or current-based, shimming will also be employed by using correction loops and surface correction coils to minimize any residual magnetic field non-uniformities remaining after passive shimming is complete.

The storage ring magnet is powered by three superconducting coils. The coils are positioned as shown in Figure 3.1. The coil at the outer radius drives the magnetic field across the storage ring gap, while the two coils at the inner radius cancel the flux in the center of the storage ring and improve the magnetic field quality in the storage ring gap. The two inner coils are located above and below the midplane of the storage ring so they do not block access to the storage region. The outer coil carries a current of 5200 A with 48 turns, and the inner coils each have 24 turns (Danby, et al. 158). The inner coils are connected in series with the outer coil, with the reverse current direction. For the E821experiment, the magnet usually operated at 5.0 K, and indirect cooling was provided by helium pipes mounted to a massive aluminum mandrel. Since the coils are wound starting from the inside of the storage ring, the coils push radially outward against the mandrel when they are powered. The E989 experiment plans to use a similar setup, and much of the storage ring and its components will be reused.

3.3 Moving the Storage Ring

The storage ring magnet for the E821 experiment was designed, constructed, and shimmed to produce a uniform magnetic field, constant to a few parts per million and measured to 0.1 ppm precision (Danby, et al. 153). The magnet is one-of-kind, and the magnetic field it produces is able to be measured with higher precision than any other magnet of a similar size. Thus, the E989 Collaboration decided to reuse the storage ring, with additional shimming to further reduce local variations in the magnetic field, and some modifications to meet higher precession needs.

Reusing the storage ring involved moving the magnet yoke, pole pieces, and superconducting coils from Brookhaven National Laboratory (BNL) in New York to Fermilab in Illinois. Although the magnet yoke and poles could be disassembled and moved across land by conventional trucks, the fourteen-meter-diameter superconducting coils had to be moved as a single unit in order to preserve the coil's ability to produce a precise magnetic field. Specialized fixtures were used to transport the coils 3200 miles on both land and water routes. First, the coils were transported by land from BNL to a port in Long Island, New York. Next, the coils traveled on a barge down the east coast, around Florida, up the Mississippi River, and through the Illinois Waterway to Lemont, Illinois. Along the eastern seaboard, the barge traveled through the Intracoastal Waterway so the barge could remain near ports where the water was calmer than on the open sea, and the time of year for the move was chosen to avoid hurricane season and winter weather. Finally, the coils were transported by land the last leg of the trip to Fermilab.

The coils were shipped in a horizontal position to minimize the forces and stresses on them. Throughout the move, the coils were kept level to within one-tenth of an inch, while the coils' circular shape was maintained to within one-quarter of an inch. The stresses on the coils were determined to be no more than a few hundred psi, which was not expected to damage the coils (Roberts, et al. 658). Emmert International moved the storage ring, and Figure 3.3 shows the 45-ton shipping fixture they designed and built to stabilize the coils during transportation. Figure 3.4 is a photograph of the coils secured in the shipping fixture, just prior to wrapping the coils in shrink wrap. Figure 3.5 is an engineering drawing of the truck and trailer used to move the coils across land. The trailer had three hydraulic zones to keep the coils level and to

distribute the weight of the load evenly to the wheels. The land route utilized four-lane roads and highways since the coils are about four traffic lanes wide. Land transportation occurred at midnight on weekends to avoid interfering with regular traffic, and the truck drove at speeds ranging from walking speed up to 10 mph. Figure 3.6 is an engineering drawing of the shipping fixture and superconducting coils anchored to a barge for water travel, and Figure 3.7 is a photograph of the superconducting coils traveling by barge. After 35 days of travel, the superconducting coils arrived at Fermilab on July 26, 2013. About 3,000 spectators attended the event dubbed the "Big Move."

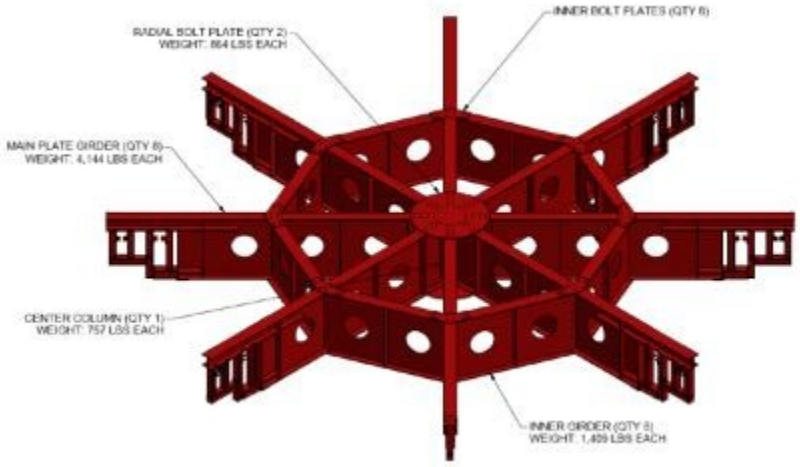

Figure 3.3: Shipping fixture for the superconducting coils. (Image courtesy of B. Lee Roberts, FNAL).

Figure 3.4: The superconducting coils secured in the shipping fixture, ready for shipment from Brookhaven to Fermilab. (Image courtesy of Brookhaven National Laboratory, BNL).

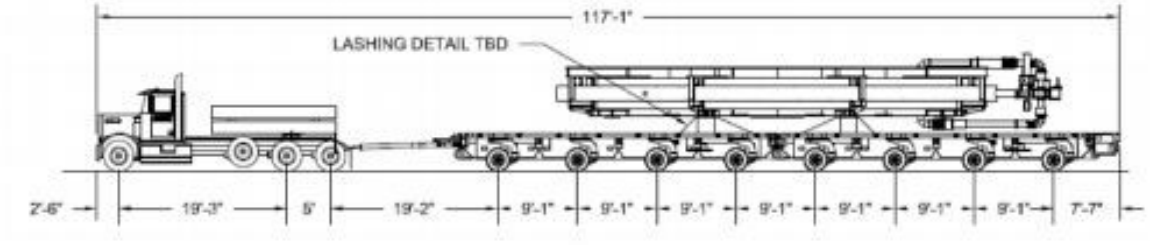

Figure 3.5: Specialized truck and trailer for coil shipment across land. (Image courtesy of B. Lee Roberts, FNAL).

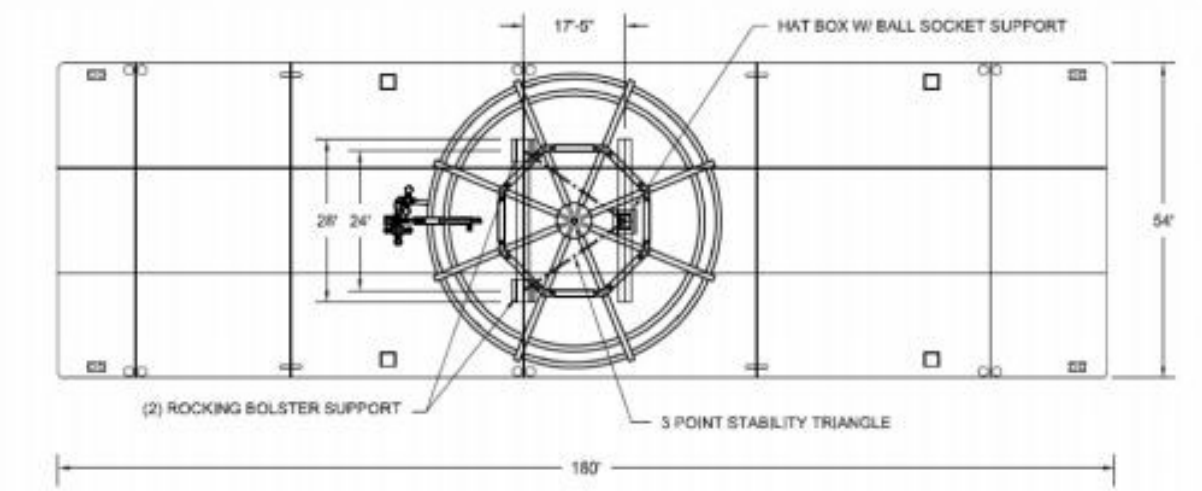

Figure 3.6: Superconducting coils, supported in a shipping fixture and anchored to a barge. (Image courtesy of B. Lee Roberts, FNAL).

Figure 3.7: The superconducting coils being transported by barge up the Tennessee-Tombigbee Waterway. (Image courtesy of Darin Clifton, Ceres Barge).

3.4 Preparations to Reconstruct the Storage Ring

Before the storage ring was relocated from BNL to Fermilab, all unpainted surfaces of the magnet yoke and spacer plates were coated with Cosmoline, a brown, wax-like rust preventative. Before final placement of the magnet in Fermilab's newly constructed MC-1 building, the Cosmoline had to be removed.

To clean the top surfaces of the yokes and spacer plates, mineral spirits were poured onto the Cosmoline and left to soak in for about two hours. Once the Cosmoline had softened, it was gently removed with flat-edged paint scrapers. Care was taken not to mar the metal surfaces so the precision achieved during manufacturing could be preserved. The initial cleaning left a tacky residue on the yoke surfaces, so more mineral spirits was applied with spray bottles, and the residue was rubbed off with Scotch-Brite™ scouring pads. Rust was removed by spraying the yoke surfaces with WD-40® Multi-Use Product and rubbing with the scouring pads. In particular, the yoke ears needed to be completely free of rust. When all unpainted surfaces were clean and free of rust, the yokes were polished with a clean terrycloth towel saturated in mineral spirits, and then coated with a thin layer of WD-40® to seal out moisture from the exposed metal.

The yokes and spacer plates could not be flipped to make the bottoms or sides face upright, so a different technique was used to clean the bottom and side surfaces. Since mineral spirits was too thin to apply over head and to the sides without it dripping off, viscous paint stripper was used instead. The paint stripper was applied with paint brushes, and sheets of waxed paper were immediately pressed onto the wet paint stripper to keep it from drying

before the Cosmoline had softened. After twenty or so minutes, the waxed paper was peeled off, taking about half the Cosmoline with it. The remaining Cosmoline was removed with flat-edged paint scrapers and Scotch-Brite™ scouring pads. As in the case with the top surfaces, rust was rubbed off with scouring pads and WD-40®. Finally, the surfaces were polished with a clean terrycloth towel soaked in mineral spirits and coated with a film of WD-40®.

After several weeks of cleaning, the yokes and spacer plates were ready to be positioned, shimmed, and bolted together. Each yoke was fastened to the adjacent yokes on the left and right with bolts through the ears. The ears are slightly recessed in comparison to the sides of the yokes, so when one yoke is flush against another yoke, a small air gap is present between the ears. The gaps vary in width from 0.05 inch to 0.1 inch. The metal shims used by the E821 experiment as part of the passive shimming process were reused for the E989 experiment. The shims were not labeled, so the thickness of each shim was measured in four places with a caliper, and the measurements were averaged. The thicknesses ranged from about 0.01 inches to about 0.09 inches. Depending on the width of the gap, combinations of one to two shims were inserted between each pair of yoke ears. The shims allow for fine adjustments to the azimuthal position of the yokes during placement, which helps ensure the magnet will be continuous, and the positions of the yokes and shims will not change throughout the experiment.

The bottom yokes and some of the spacer plates were placed the summer of 2014. The magnet is supported at the joints between the bottom yokes by four 25 ton Duff Norton worm gear screw jacks. The jacks are on top of base plates made of 7.6-inch-thick steel. The base plates are bolted and grouted to the cement floor in MC-1, and their positions were measured

by a team of surveyors. The base plates also hold massive angle brackets with adjustment screws to move the yoke ends radially. Figure 3.8 shows the yoke placement in progress in MC-1. In the photograph, eleven of the twelve bottom yokes and two of the spacer plates (bottom half only) have been placed. The base plates and massive angle brackets are also visible. The placement and shimming of the pole pieces and the remaining yokes and spacer plates will continue over the next year.

Figure 3.8: Yoke placement in progress in the MC-1 building at Fermilab. (Image courtesy of Scott Walstrom, NIU).

CHAPTER 4

TRACKING DETECTORS

4.1 Introduction

The muon anomalous spin precession frequency, ω_a, and the value of the magnetic field normalized to the Larmor frequency of a free proton, ω_p, are the two frequencies measured experimentally to obtain the muon anomalous magnetic moment, a_μ. To ensure the E989 experiment's goal of 140 ppb precision on a_μ, the error budget allows for a 100 ppb statistical uncertainty overall, with equal 70 ppb systematic uncertainties on the analyses of ω_a and ω_p. Since Pulsed Nuclear Magnetic Resonance (NMR) can measure magnetic fields to absolute accuracies of tens of part per billion, NMR probes will be responsible for measuring ω_p. The straw tube tracking detectors and calorimeters will be responsible for measuring ω_a.

The E989 experiment will begin taking data in 2016, and for the first two year run, polarized beams of positively-charged muons will be injected into a storage ring containing a uniform magnetic field, where the muons' spins will precess at a different rate than their momenta. Direct measurement of the muon spin is not feasible; instead, indirect measurement of the muon spin will be performed using positrons produced in the decay of positive muons. Muons decay via the weak interaction, so the decay violates parity. As a result, the momenta

of the emitted positrons carry information about the spin directions of the parent muons, and the highest energy positrons are emitted in the direction of the underlying muon spin. Therefore, indirect measurement of the muon spin is obtainable by measuring the modulation in the energy spectrum of the decay positrons. By applying a 1.8 GeV energy cut to the bin data for the number of positrons versus time in the fill, a "wiggle" plot emerges for ω_a. Figure 4.1 shows the resulting arrival-time spectrum from the final E821 data run in 2001, where the requirement that the positrons have at least 1.8 GeV of energy caused ω_a to oscillate similar to a sine wave.

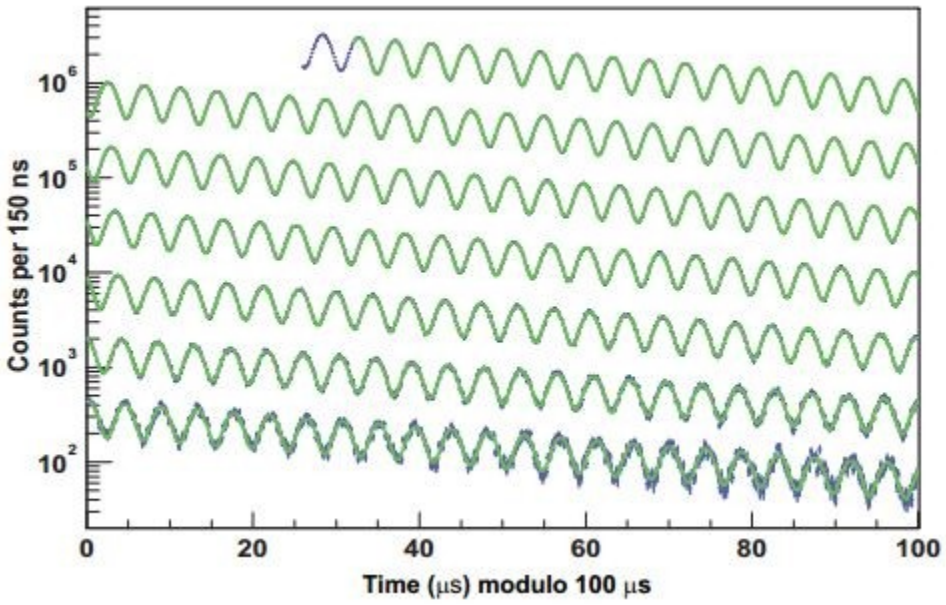

Figure 4.1: The number of detected positrons divided by 1.8 GeV of energy and versus the time in the fill. The data is shown in blue, and superimposed to the spectrum is a least-squares fit shown in green. (Image courtesy of B. Lee Roberts, FNAL).

In the E989 experiment, twenty-four electromagnetic calorimeters located equidistant around the storage ring will measure the energy and time of arrival of the daughter positrons. Tracking detectors located in front of three of the calorimeters will perform a number of tasks,

including measuring the muon beam profile as a function of time throughout the muon fill, verifying systematic uncertainties in measurements made by the calorimeter, and analyzing the tilt in the muon precession plane. More about the tracking detector goals is described below. Ultimately, the tracking detectors will provide ppm level corrections to the measurement of ω_a and validate the results from the calorimeters so a precise value for ω_a can be obtained.

4.2 Physics Goals

The straw tube tracking detectors for the E989 experiment will accomplish three main goals. First, the tracking detectors will measure the muon beam profile at three locations around the storage ring as a function of time throughout the muon fill. Second, the tracking detectors will provide an independent verification of the systematic uncertainties derived from the calorimeter data. Lastly, the tracking detectors will furnish evidence showing whether or not the muon precession plane has tilted away from the vertical direction. Note, a tilt in the precession plane indicates a radial or longitudinal component to the magnetic field or a permanent muon electric dipole moment, any of which compromises the precision in a measurement of ω_a.

To achieve the three goals and constrain systematic uncertainties, the tracking detectors will fulfill several roles. First, in regard to measuring the muon beam profile, the tracking detectors will measure the muon beam profile on a fill by fill basis to ensure proper beam alignment and reduce systematic uncertainties in the measurement of the average magnetic field seen by the muons. The tracking detectors will also measure the beam

oscillation parameters as a function of time in the fill to reduce systematic uncertainties in the beam dynamics corrections. Second, to validate the reduced systematic uncertainties in data collected by the calorimeter, the tracking detectors will provide a check on the calorimeter-based pileup correction by isolating time windows where more than one positron hits the calorimeter. Additionally, the tracking detectors will provide a check on the calorimeter-based gain measurement by measuring the positron momentum with better resolution than attainable with the calorimeter. Third, to determine how much the muon precession plane has tilted away from the vertical, the tracking detectors will measure the up-down asymmetry in the positron decay angle. Only the tracking detectors are able to measure the asymmetry, and systematic uncertainty in the asymmetry measurement will be minimized by the large acceptance and statistics anticipated for the E989 experiment.

4.3 Design Requirements

In order for the tracking detectors to fulfill the roles described in section 4.2 and meet the demands of measuring the muon anomalous spin precession to a statistical error of 100 ppb, while restricting systematic uncertainties to the 70 ppb level, the design of the tracking detectors must satisfy several requirements:

- First, the DC nature of the stored muon beam requires the tracking detectors to perform well for both a large momentum range and for muon decay positions beginning up to 10 meters before the first tracking plane in front of the calorimeter.
- Second, the tracking detectors must be able to measure the vertical and radial muon beam profile to much better than 1 cm, meaning the detectors must have on the order

of 100 μm resolution per position measurement in the storage ring's radial direction. The resolution requirements are relaxed, though, in the vertical direction because no curvature in the muon beam profile occurs.

- Third, long extrapolations from the tracking detector to the muon decay point means multiple scattering must be minimized, and the material comprising each tracking plane must be below 0.5% the radiation length.
- Fourth, the tracking detectors must be in a vacuum of about 10^{-6} Torr, with a vacuum load on the system below 5×10^{-5} Torr l/s.
- Fifth, to detect the largest number of positrons, the tracking detectors must be pushed as close as possible in the radial direction to the stored muon beam without entering the storage region or interfering with the NMR trolley track.
- Sixth, passive material in the vertical direction must be at least ±4.5 cm from the beam center so the positron measurements downstream in the calorimeter are not degraded.
- Seventh, the tracking planes must be as close together as possible to maximize acceptance of low momentum positrons.
- Eighth, the first and last tracking planes must be as far apart as possible so the lever arm is long enough to extrapolate high momentum positrons back to the muon decay point.
- Ninth, perturbations to the magnetic field caused by DC current or material in the tracking detectors must be less than 10 ppm at the center of the storage region over an azimuthal angle greater than 2°.

- Tenth, any perturbations to the magnetic field caused by transient currents on timescales less than 1 ms must be below 0.01 ppm because transient currents below 0.01 ppm are invisible to the NMR system.

To meet the design requirements and unprecedented precision goals of the E989 experiment, the tracking detectors will be newly constructed, rather than reused or modified from the E821 experiment. Due to the DC nature of the stored muon beam, the tracking detectors will contain multiple planes spread over as long a lever arm as possible. Also, the detectors will be gas based to accommodate the required number of planes with a minimum of multiple scattering. The tracking detectors will be housed within a vacuum to further minimize multiple scattering. Thus, straws will be used because the circular geometry can maintain the differential pressure with a minimal wall thickness. Thin walls for the straws are desired to reduce the amount of material the positrons must travel through in the measurement process.

4.4 Tracking System Design

The entire storage region will be enclosed in a continuous vacuum. The walls of the vacuum will be reused, with modifications, from the E821 experiment, and are composed of a set of twelve aluminum vacuum chambers joined together. When a muon decays, the decay products do not have enough energy to continue traveling on the magic orbit within the storage ring, so the trajectories of the decay products curl in toward the center of the ring. Therefore, each vacuum chamber contains two scallop regions, for a total of twenty-four scallop regions in the entire vacuum, where tracking detectors can be placed to make

measurements of the daughter positrons. The newly constructed tracking detectors will be placed in three of the scallop regions, and calorimeters will sit just outside the vacuum at the widest end of all twenty-four scallop regions.

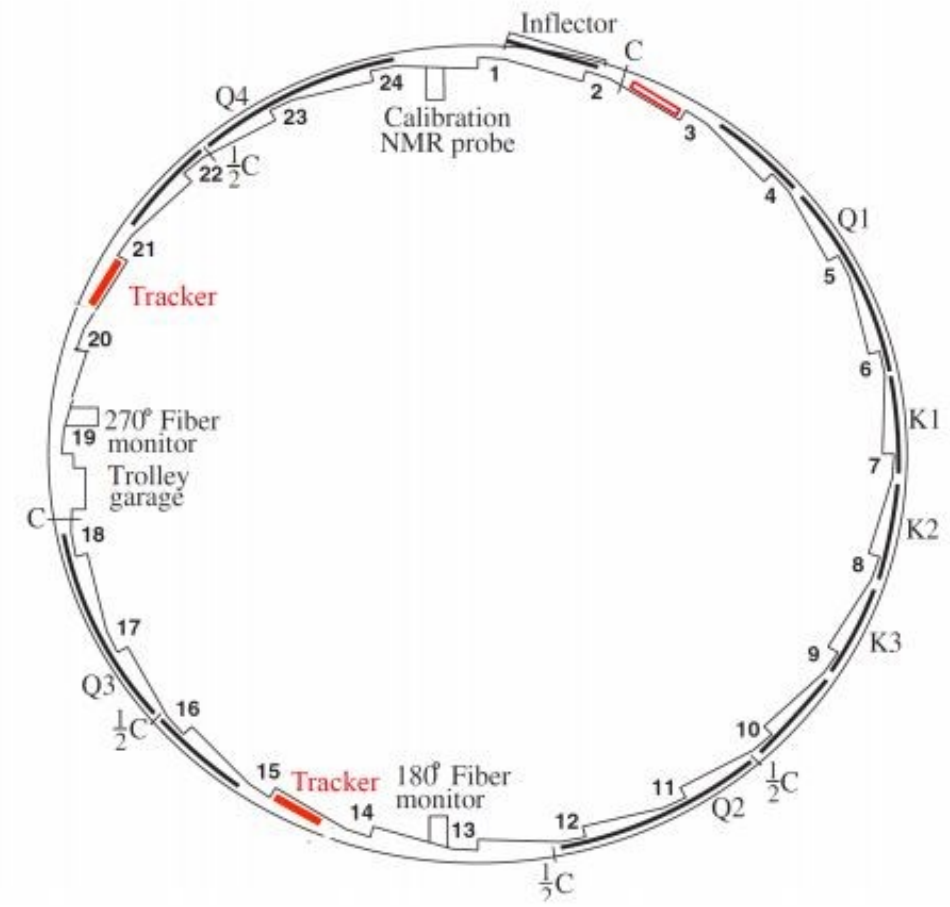

Figure 4.2: Twelve aluminum vacuum chambers joined together enclose the muon storage region. Each vacuum chamber contains two scallops. Calorimeters will be placed just outside all twenty-four scallops. Tracking detectors will be placed in front of the calorimeters inside scallops 3, 15, and 21, as shown in red above. The kickers are labeled K1-K3, the quadrupoles are labeled Q1-Q4, and the collimators are labeled "C" or "½C," depending on whether the collimator covers the full aperture or half aperture. The muon beam circulates the vacuum in the clockwise direction. (Image courtesy of B. Lee Roberts, FNAL).

Muons enter the storage region shown in Figure 4.2 at the inflector and circulate the storage ring in the clockwise direction. The kickers (K1-K3) put the muons on the magic radius, while quadrupoles (Q1-Q4) provide vertical focusing of the muon beam. The collimators ("C" or "½C," depending on whether the collimator covers the full or half aperture) remove muons located outside the 9 cm diameter of the storage region, and the design of the collimators is intended to have as little effect as possible on the decay positrons. Several hundred fixed NMR probes located just above and below the muon storage volume continuously monitor magnetic field changes at the edges of the storage volume, and a trolley holding an array of seventeen NMR probes travels around the ring on a track inside the vacuum chambers. Without ever breaking the vacuum, the NMR trolley pulls out of its garage once every two to three days while the beam is off for about two hours, circulates the storage ring to measure the magnetic field distribution at 6000 points over the muon storage region, and then pulls back into its garage. The four fiber harps are frames, strung with seven scintillating fibers each, which can be rotated into the storage region to make a direct, but destructive, measurement of the distribution of stored muons and the associated beam dynamics parameters. The fiber harps will be grouped in pairs at two locations, and they will determine the position (x, y) and angle of the muon beam both when the beam was injected into the storage ring and during the kick phase. The fiber harps will also characterize the periodic muon beam motion, especially modulation of the beam centroid position and width caused by coherent betatron oscillations. In the E989 experiment, calorimeters will be located just outside the widest end of all twenty-four scallop regions. Tracking detectors will be in front of the calorimeters inside the vacuum of scallops 3, 15, and 21, as indicated by the red in

Figure 4.2. The location of the tracking detectors was chosen so the muon beam seen by the detectors would be unobstructed by quadrupoles and collimators.

The tracking detectors in one scallop region comprise a tracking station, and each of the three tracking stations shown in Figure 4.2 will contain nine tracker modules. The tracking stations will contain three types of modules with different numbers of straws, depending on the maximum number of straws able to fit within each scallop without entering the muon storage region. The modules are referred to as "type-32," "type-24," and "type-16," where the type indicates how many straws are located in each row of the module. Figure 4.3 shows how the modules are arranged in a single tracking station. Each tracking station will have four type-32 modules closest to the calorimeter where the scallop is the widest. Adjacent to the type-32 modules will be three type-24 modules, and furthest from the calorimeter will be two type-16 modules. Closer to the calorimeter the modules will have more straws in each row to maximize coverage of the calorimeter and potentially increase acceptance, as discussed further in section 5.3. For modules further from the calorimeter, fewer straws fit in each row due to the shape of the scallop region.

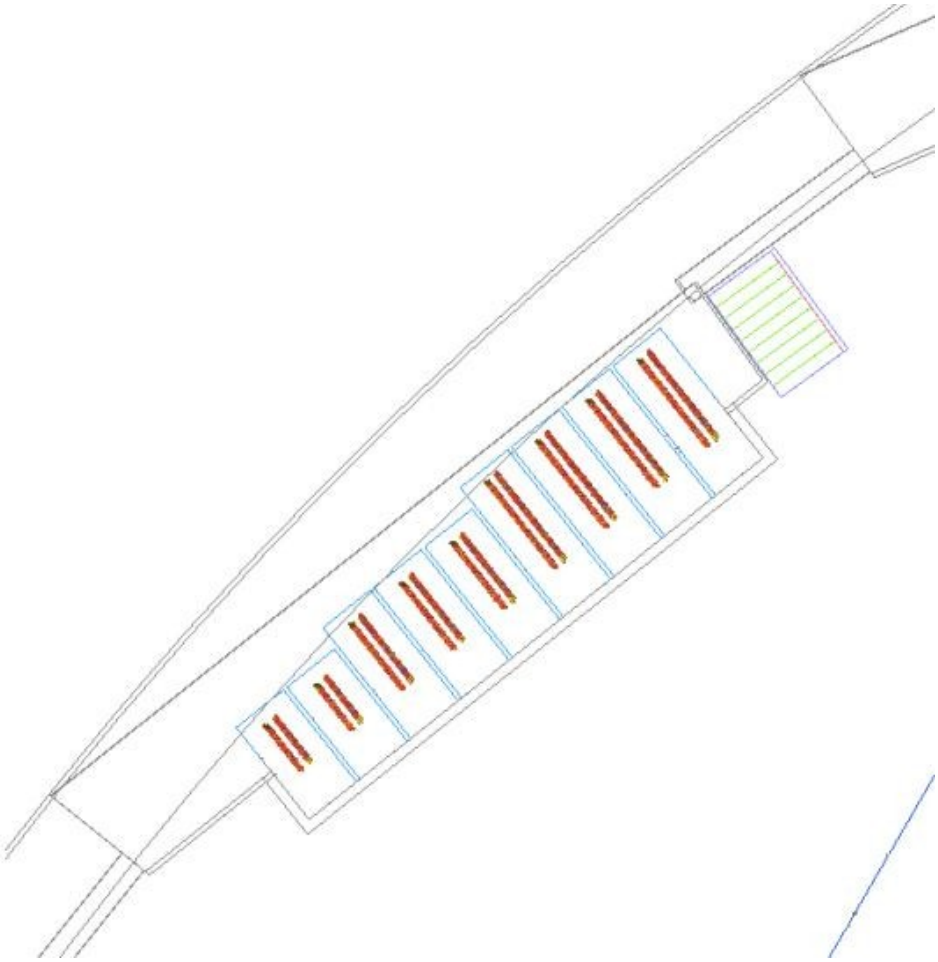

Figure 4.3: A single scallop region, showing how the modules are arranged within the tracking station. Each tracking station contains nine modules: four type-32, three type-24, and two type-16, where the type indicates the number of straws in each row. (Image courtesy of B. Lee Roberts, FNAL).

Table 4.1: Required number of straws for the tracking detector system.

Module type	Straws per module	Modules per station	Spare modules per station	Total straws per station
Type-32	128	4	1	640
Type-24	96	3	1	384
Type-16	64	2	1	192
Total straws per station				1216
Total straws for 3 stations				3648

Each module contains four rows of straws grouped together in two closely-packed doublet planes, where the planes are oriented at ±7.5° from the vertical direction. The plane with the negative slope is the U plane, and the plane with the positive slope is the V plane. The wire inside each straw can only register a positron hit, not the exact location of the hit along the length of the wire. Thus, the 15° angle between the U and V planes allows for both the vertical and horizontal positions of the positron hits to be determined. Since each module has four rows of straws, the type-32 module has 128 total straws, each on a separate channel. The type-24 module has 96 channels, and the type-16 module has 64 channels. The total number of straws, plus spares, needed for three tracking stations is given in Table 4.1. Each tracking station will have one spare module for each module type.

4.5 Straw Design

Figure 4.4 shows the dimensions of the proposed straw for use in the current design of the tracking detectors. The total straw length, including endpins, is 116 mm, and the straws are 5 mm in diameter. The straw walls are made of two layers of 6 μm Mylar, spiral wound and glued together with a layer of 3 μm adhesive between the layers. To form a cathode layer, the inside of the straw has 500 Å layer of aluminum overlaid with a 200 Å layer of gold. For additional electrostatic shielding and a slower leak rate, the outside of the straw is coated with a 500 Å layer of aluminum. Including the Mylar, coatings, and adhesive, the total thickness of the straw is 15 μm.

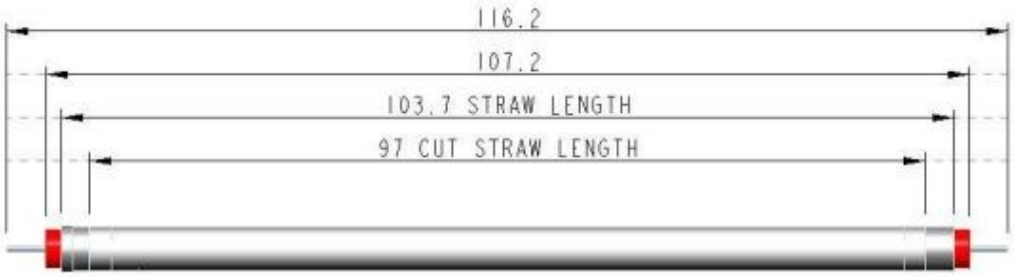

Figure 4.4: Proposed straw for use in the tracking detectors. All dimensions are in millimeters. (Image courtesy of John Carroll, University of Liverpool).

Aluminum end-pieces will be glued into both ends of the Mylar straws using a combination of silver and structural epoxies. The aluminum end-pieces will provide electrical contact between the straws and the aluminum manifolds, while holding the straws in place inside the modules. The end-piece on the right in Figure 4.4 is designed to fit through the holes in the manifold, whereas the end-piece on the left has a "top hat" to prevent it from fitting through the manifold holes. The two different types of end-pieces simplify assembly of the modules and tensioning of the straws. Figure 4.5 shows an end-piece with the "top hat." The groove in the end-piece will hold epoxy.

Red plastic inserts will be slid into the ends of the aluminum end-pieces, and the inserts will be molded around crimp pins. A gold-plated tungsten wire, 25 μm in diameter, will be strung through each straw, and the crimp pins will center the wire within the straw and hold the wire under 10 grams of tension. The crimp pins also provide an electrical connection to the first stage electronics. Figure 4.6 is a cross-section of an assembled straw. The wire length inside the straw is 80.2 mm. Figure 4.7 shows detail of a straw end, and Figure 4.8 is a drawing of a crimp pin in a plastic sleeve. Slots in the plastic inserts will allow gas to flow through the straws, and the drift gas will be 80% Argon and 20% CO_2. The option of

flammable gas is also being explored because the electronics may need to be moved outside the manifolds due to insufficient space inside the manifolds. If the electronics are further from where the positrons hit the wires, the gain will need to be increased to compensate for a decreased signal to noise ratio. Historically, argon ethane has been used to give a higher gain with better resolution. The wires inside the straws will be held at a voltage of 1500 V.

Figure 4.5: A computer drawing of an aluminum end-piece designed to provide an electrical connection between the straw material and the aluminum manifolds holding the straws in place. (Image courtesy of John Carroll, University of Liverpool).

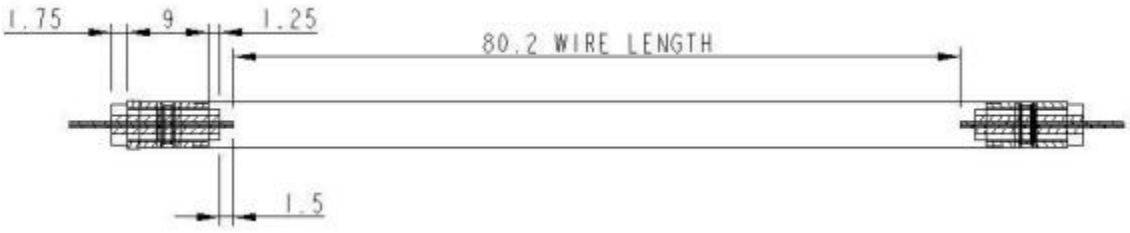

Figure 4.6: Cross-section of assembled straw with aluminum end-pieces, plastic inserts, and crimp pins. All lengths are in millimeters. (Image courtesy of John Carroll, University of Liverpool).

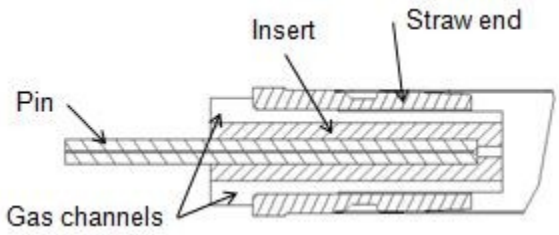

Figure 4.7: End detail of a straw. The pin crimps the wire inside it, and plastic inserts hold the crimp pins in place. The plastic inserts contain slots for gas to flow through the straws. (Image courtesy of John Carroll, University of Liverpool).

Figure 4.8: Crimp pin and red plastic sleeve. (Image courtesy of John Carroll, University of Liverpool).

4.6 Manifold Design

The manifolds for the tracking detectors will provide structural support by holding the straws in place. The manifolds will also house the first stage electronics and have inlets/outlets for electrical connections, gas pipes, and the water cooling system. Three manifold sizes in varying widths will be constructed, one size each for the type-32, type-24, and type-16 modules. Figure 4.9 shows a schematic of the current design for the type-32 module. The upper and lower manifolds are made of aluminum, and they are supported by a flange on one end and a carbon fiber post on the opposite end. Each manifold pair holds four

rows of straws arranged in one doublet U-plane and one doublet V-plane. The U+V active area of the straws for the type-32 module is shown by the red outline in Figure 4.10. At the widest point, the U+V active area is 196 mm for the type-32 module, 148 mm for the type-24 module, and 100 mm for the type-16 module. For the all three module types, the height of the U+V active area is 82 mm. Indium seals will be used to provide vacuum tightness between the manifold lid and body and at the points where the upper and lower manifolds bolt to the flange. The flanges will face toward the center of the storage ring, and the fully assembled modules will be inserted one at a time into the vacuum region scallop. The nine modules in each tracking station will be packed close, as shown in Figure 4.11, and the interleaved bolt patterns between adjacent flanges allow space for vacuum seals. During assembly, the modules will undergo several quality control tests to ensure all components are working. After the modules are assembled, but before insertion into the vacuum chambers, the modules will also undergo a systems test using cosmic rays or a radioactive source to verify proper functioning of all channels.

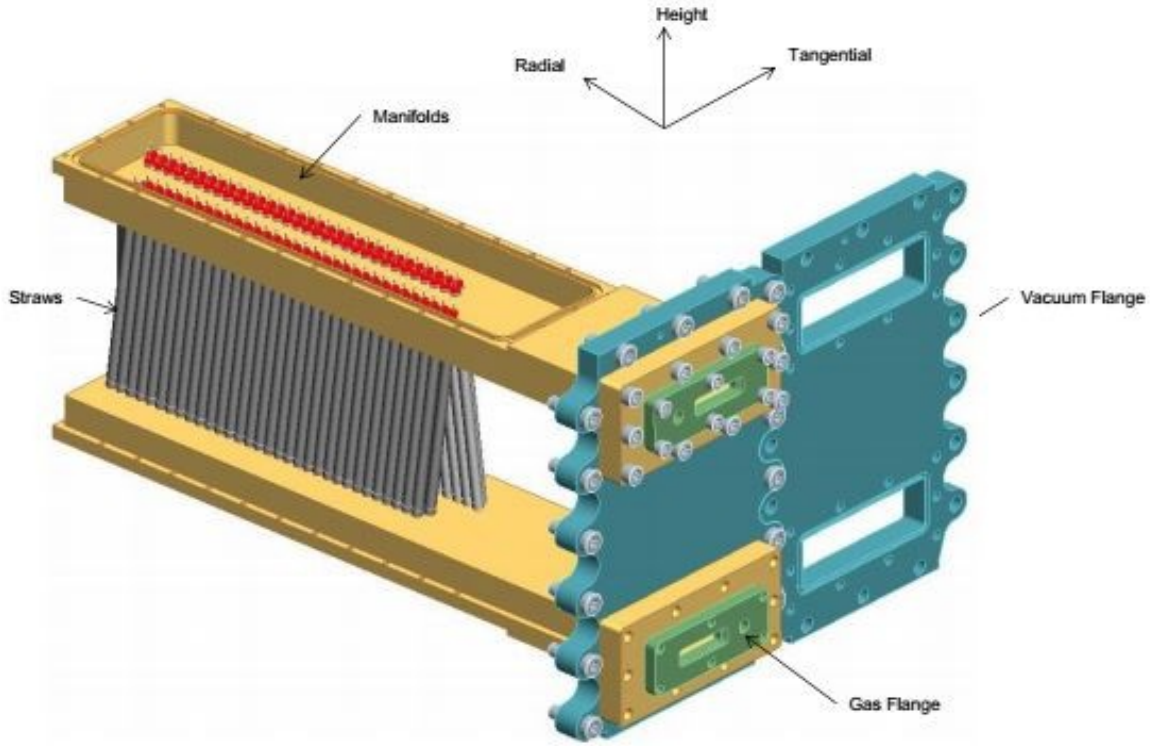

Figure 4.9: Type-32 module containing four rows of straws arranged in one doublet U-plane and one doublet V-plane. The straws are held in place by upper and lower aluminum manifolds, shown in tan. The manifolds are mounted to a flange, shown in blue, and a carbon fiber post at the opposite end of the module offers additional structural support. Gas will be distributed independently to each module with the supply entering through the flange in the top manifold and exiting through the flange in the bottom manifold. (Image courtesy of John Carroll, University of Liverpool).

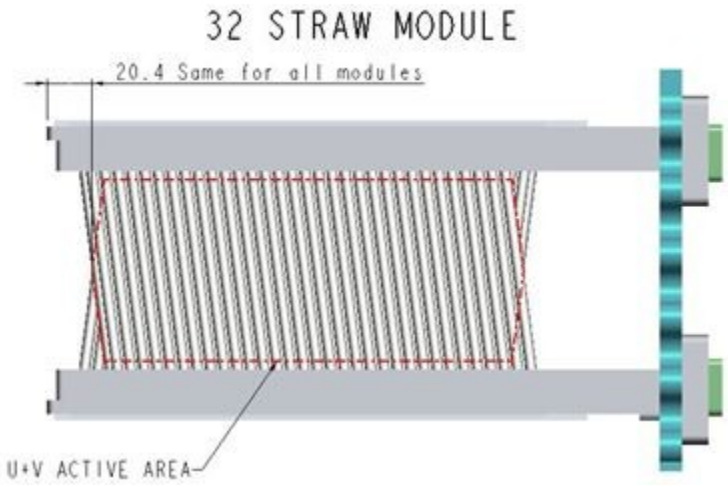

Figure 4.10: U+V active area, outlined in red, for the type-32 module. (Image courtesy of John Carroll, University of Liverpool).

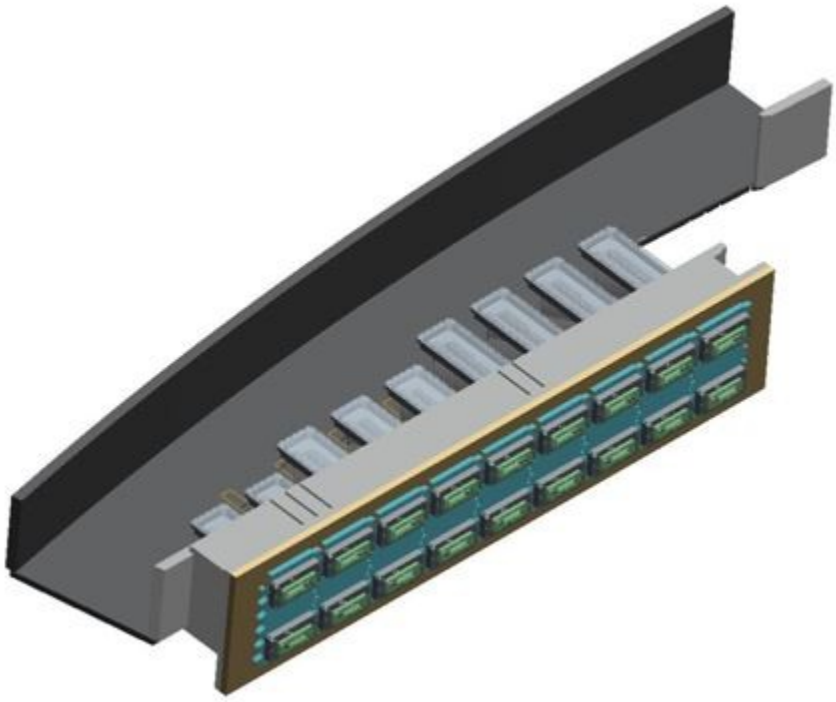

Figure 4.11: Nine modules inserted into the vacuum region scallop to form a tracking station. (Image courtesy of John Carroll, University of Liverpool).

4.7 Modifications to the Vacuum Chamber

As design of the tracking detector system progressed, the vacuum chamber appeared to need modifications in order to accommodate the design changes for the E989 experiment. In particular, the vacuum chamber did not have enough space for insertion and alignment of the straw tube tracking detectors, so modifications were deemed necessary. Three factors influenced the proposed modifications. First, was the goal to fill as much space in the vacuum chambers as possible with tracking detectors. Second, in the event of a malfunction or defect, an individual module needs to be quickly and easily replaced with a spare. Third, the modules need to attach directly to the flange to simplify insertion of the modules into the vacuum chamber and maintain alignment of the modules. All three factors lead to a need for the flanges to have bolts outside the original vacuum chamber height. The vacuum chamber height, however, is constrained by the magnet and pole pieces. Therefore, the decision was made to extend the vacuum chamber radially in toward the center of the storage ring, beyond the magnet and pole pieces. A lip welded onto the edge of the extension will provide sufficient height for the flange bolts. The extension will also provide sufficient space for the tracking detectors to be inserted and aligned in the vacuum chamber. In fact, the extension even provides enough space in the radial direction for the positions of the modules to be adjusted, or for the manifolds to be made longer to accommodate more straws. As discussed in chapter 5, simulation was used to test different module types in various configurations. In Figure 4.12, the top picture shows one section of the original vacuum chamber, and the

bottom picture shows the same section with the proposed extension welded to the scallop region on the left.

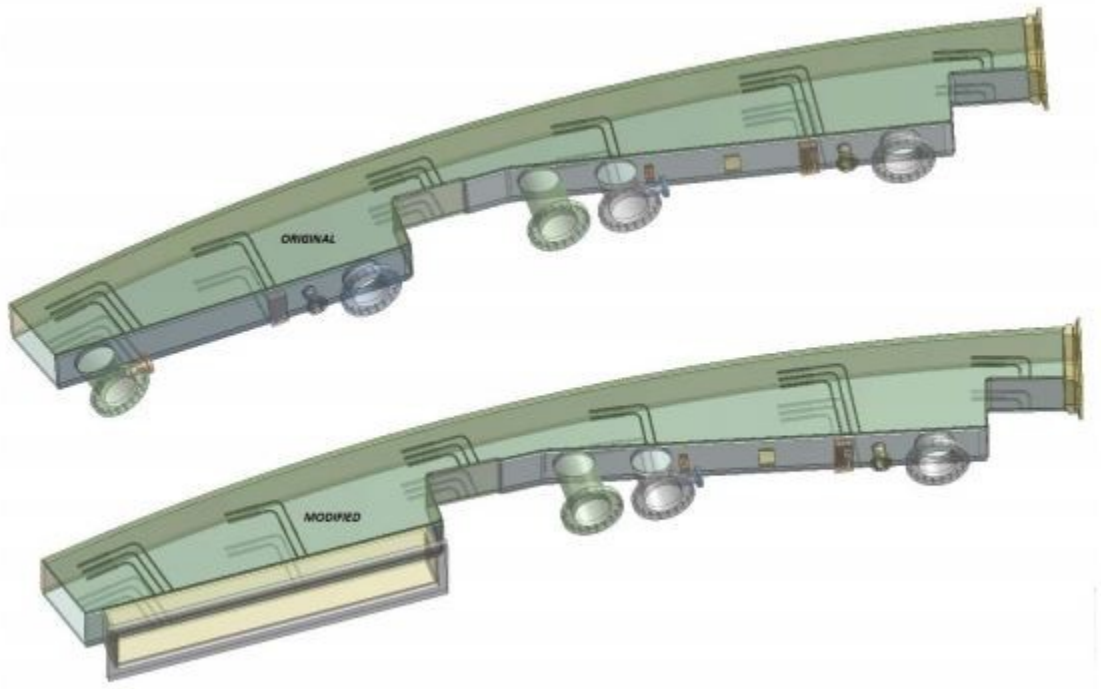

Figure 4.12: Original and modified versions of one section of the vacuum chamber. The bottom picture shows an extension added to the scallop region on the left. (Image courtesy of B. Lee Roberts, FNAL).

CHAPTER 5

TRACKER SIMULATION

5.1 Introduction

The simulation code for the E989 experiment utilizes the ART software framework (https://cdcvs.fnal.gov/redmine/projects/art). The ART system contains the code infrastructure and includes a universal, reusable software environment for all E989 code developers to share. The general functionality provided by ART allows developers to focus on writing physics code, rather than spend limited time and resources on designing and writing the foundation for a complicated new system. Also, sharing code and reproducing consistent results is easier with ART, and ART has both a build system and a Release, Dependency, and Environment management system. The management system keeps track of compatibility between the various libraries and code versions, helping to ensure consistent builds where all the code compiles with the same compiler and the same compiler options.

One reason the E989 simulation group chose the ART system is because ART is modular, meaning developers independently write relatively small sections of code, called modules, containing everything necessary to execute one aspect of a desired functionality. The modules piece together within the ART framework, and they are incorporate into the program through interfaces. Each module has a discrete function, separate from other

modules, and the modules do not interact with each other, except via the ART event to achieve a program's purpose. Unlike a more traditional monolithic design, where the smallest component of code is also the whole, the modules in a modular system are built and compiled separately and can be reused without change in a variety of applications.

Although modules do not directly communicate with each other, all modules are able to read data from the ART event. The data input source could, for example, be a ROOT file, or it could be empty, as at the start of simulated data. Since ART is a ROOT-based (http://root.cern.ch/drupal/) data format and uses ROOT for data storage, the output modules make and write out ROOT histograms and ROOT trees. Most of the analysis, however, will be performed within ART so the results can be shared and reproduced without a creating an overgrown "ecosystem" based on ROOT trees.

ART uses three basic types of modules: producers, analyzers, and filters. Producers put data into the event. The new event data can be created from scratch, or derived by running algorithms on existing data. Analyzers extract data from the event and analyze it without changing any data in the event. Analyzers do not add or save data to the event, but they can write data to outputs, such as histograms, ntuples, or text files. Filters are analyzers, except they return a Boolean value. If the return value is false, then downstream modules may be prevented from running.

Globally accessible objects are managed by ART as services. Some services, like the TFileService and the RandomNumberGenerator, are provided by ART. Other services, like a geometry service, must be written and maintained by E989 code developers. Both types of services are ordinary C++ objects, and they make the same object available to all modules.

Since modules must interact via the ART event, they are forbidden to communicate with each other through services. Furthermore, services cannot call code in modules, but they can hold data and state. The schematic in Figure 5.1 shows how the basic types of modules interact with the services and the ART event.

The fcl directory houses run-time configuration files called fcl files. The fcl files tell ART what modules to load, how to run the modules, and what parameters to use during the run. The fcl files are written by developers using the Fermilab Hierarchical Configuration Language (FHICL), and they are convenient for run-time applications because fcl files can be changed and immediately run without having to rebuild the code, as in the case of making changes to modules.

5.2 Skeleton Code Structure

Development of the simulation code for the E989 experiment is currently in progress. To help organize the contributions written by several developers, a skeleton code structure was proposed. An overview of how the proposed tracking code flows is shown in Figure 5.2. The right rectangles (colored pink) represent analyzer modules, and the oblique rectangles (colored orange) represent data objects.

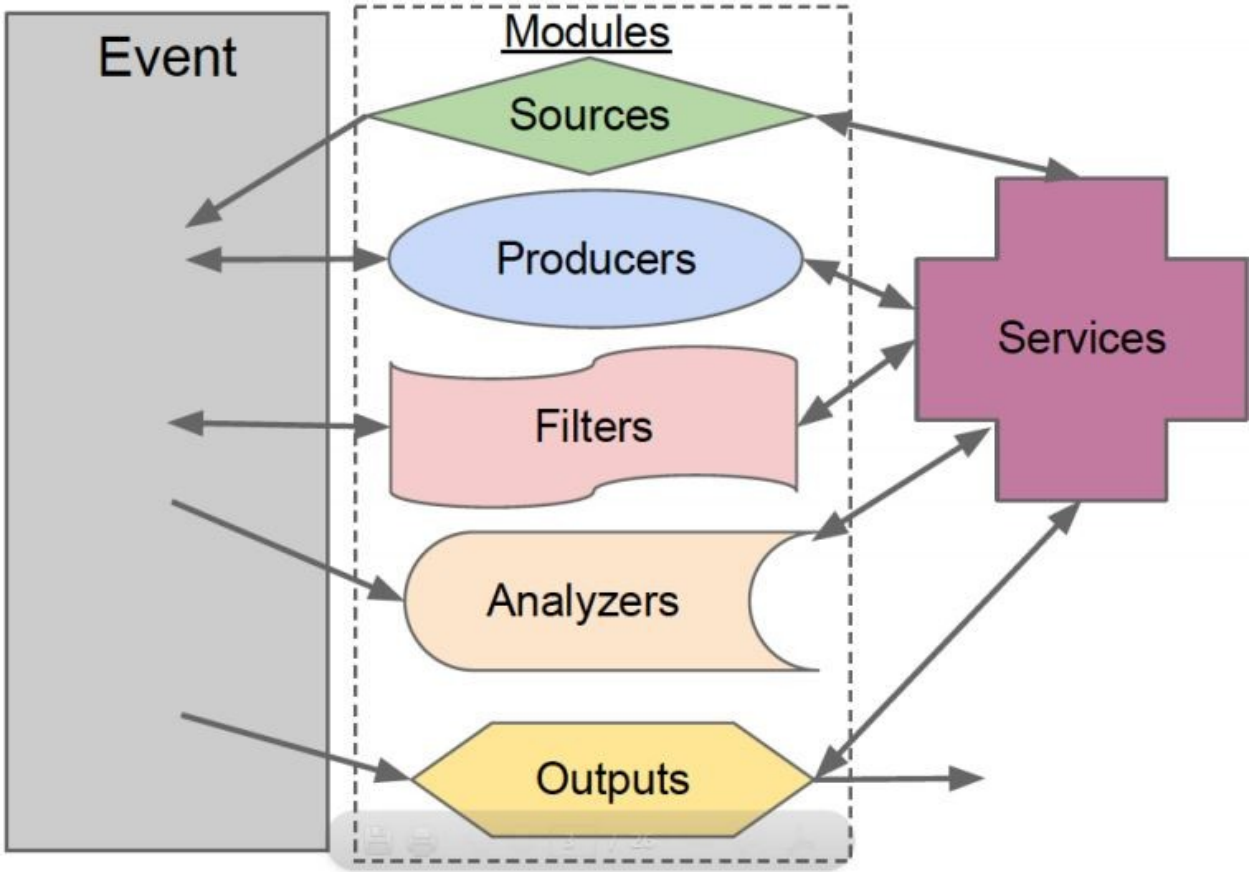

Figure 5.1: The different types of ART modules must interact with each other via the ART event. The modules can also interact with services, but they cannot communicate with each other through services. (Image courtesy of Adam Lyon, FNAL).

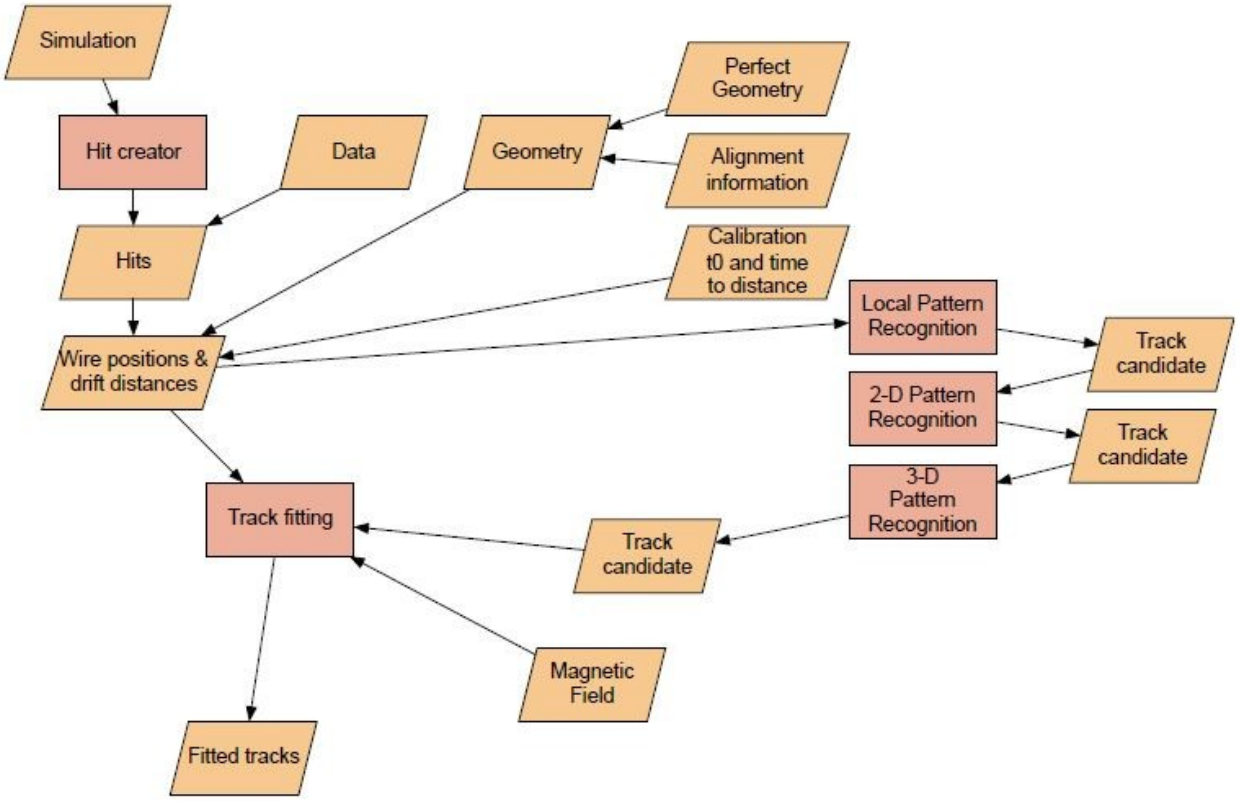

Figure 5.2: Tracking code flow chart. Right rectangles (pink) represent analyzer modules, and oblique rectangles (orange) represent data objects. (Image courtesy of Heidi Schellman, Northwestern University).

The hit creator module on the left in Figure 5.2 inputs simulation code to generate raw hits. By including data, the raw hits are converted to data hits. Data hits communicate with the geometry service to obtain the hit positions in spatial coordinates and output geometry hits. The geometry of where the straws, wires, manifolds, and other tracking detector components are physically located depends on the perfect geometry configuration and the alignment of the tracking detectors. The perfect geometry is the exact design locations of the tracking detector parts and pieces. The actual geometry, called “geometry” in Figure 5.2, will be close to the perfect geometry, but it will depend on physical measurements. The actual geometry also

depends on an alignment performed after the tracking detectors are installed in the vacuum chamber. In the alignment, real tracks are used in the tracking detectors, and then statistical procedures help minimize track residuals and determine the wire locations.

The wire positions and drift distances are derived from a combination of the geometry hits and the calibrations. The calibrations encompass the start time t_0, which is the time required for the particle to reach the tracking detector, and the time-to-distance relation. The wire positions and drift distances are fed into the track fitting module and the pattern recognition modules. The pattern recognition modules determine which hits belong to a track, and they output track candidates in three steps. First, the hits are put into the local pattern recognition module to output a one-dimensional track candidate in local coordinates. The track candidate is then put into the 2-D pattern recognition module to output a track candidate in one plane, either the U-plane or the V-plane. Finally, the track candidate is put into the 3-D pattern recognition module to obtain a track candidate with both planes.

The three-dimensional track candidates, the wire positions and drift distances, and information about the magnetic field in the vacuum chamber are inputs for the track fitting module, which does a track fit on the track candidates to find the trajectory of the particle and the parameters, such as momentum, of the particle's trajectory. The fitted track output can then be converted from local coordinates to global coordinates, and the parameters of the track can be used to extrapolate back to determine the point of tangency where the track of the positron beam is tangent to the muon beam orbit radius.

Shell scripts have been written to create skeleton code for many of the module types, and as the simulation code advances, details are added to the shell scripts and more modules are written.

5.3 Geometry Acceptance Study

One of the goals of the tracking simulation code was to make the placement and geometry of the tracking detectors as flexible as possible. A flexible code allows design changes and tests, such as a geometry acceptance study, to be implemented by modifying run-time parameters, rather than rewriting huge sections of code. In the geometry acceptance study, different configurations of the tracking modules within a single tracking station were tested to determine the optimal configuration based on how many positrons out of the total number of events passed the criteria specified in the fcl files. In particular, the file called find-and-make-golden-trackerevts.fcl was used to choose the minimum number of modules the positron was required to hit, and whether or not the positron was required to hit the calorimeter. Other fcl files were used to specify which scallop regions contained tracking stations, the geometry of the modules, the module sizes and other module parameters, and the total number of events per run. Analyzers and filters were run on the results to perform further data analysis.

For the acceptance tests, a "perfect" positron was defined to be a positron created by the decay of muon with momentum p_{magic}. A "good" event was defined as occurring when a perfect positron hit the required number of tracking modules and/or the calorimeter, as specified in the fcl files. Five different configurations of the tracking modules were

considered. The first configuration, called the Baseline, is pictured in Figure 5.3. The Baseline was the initial module configuration chosen after the decision was made to add extensions onto the three scallop regions containing tracking detectors. As shown in Figure 5.3, the Baseline configuration consists of four type-32 modules, three type-24 modules, and two type-16 modules. Schematics of the three module types are shown in Figure 5.4. Although the length of the manifolds is different for each module type, the length of the extension arm between the manifold and the flange is 61.6 mm for all three types, as indicated by the measurements in the AutoCAD drawing of Figure 5.5. Between the modules and the trolley track is 40-60 mm of unused space, depending on the module type and the module's position in the vacuum chamber. Having straws closer to the trolley track and the muon storage region,

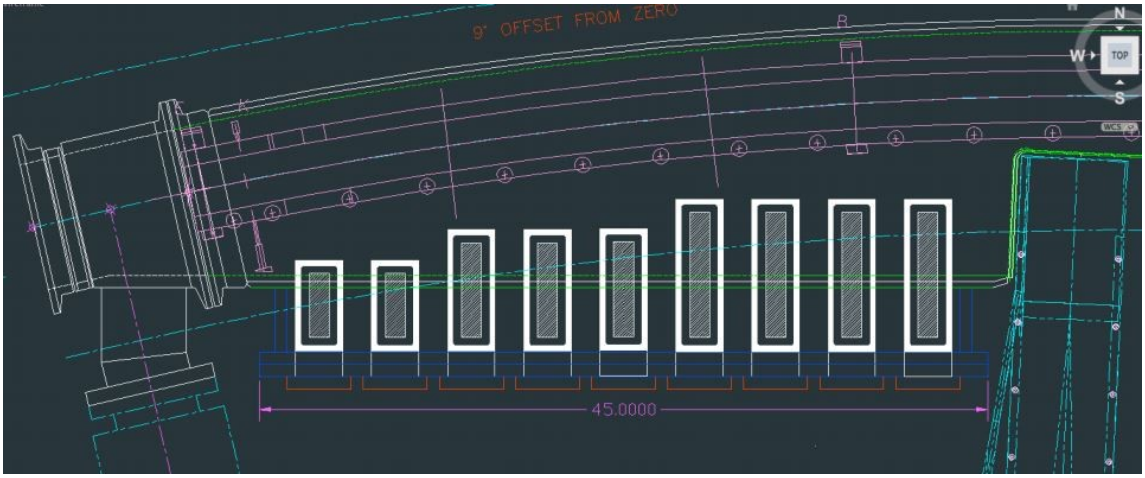

Figure 5.3: Baseline configuration for the geometry acceptance study. The modules are four type-32 modules, three type-24 modules, and two type-16 modules. All the modules have an extension arm 61.6 mm in length. The curved purple line just below the purple circles enclosing plus signs is the inside edge of the NMR trolley track. Between the modules and the trolley track is 40-60 mm of unused space, depending on the module. (Image courtesy of Leah Welty-Rieger, Northwestern University).

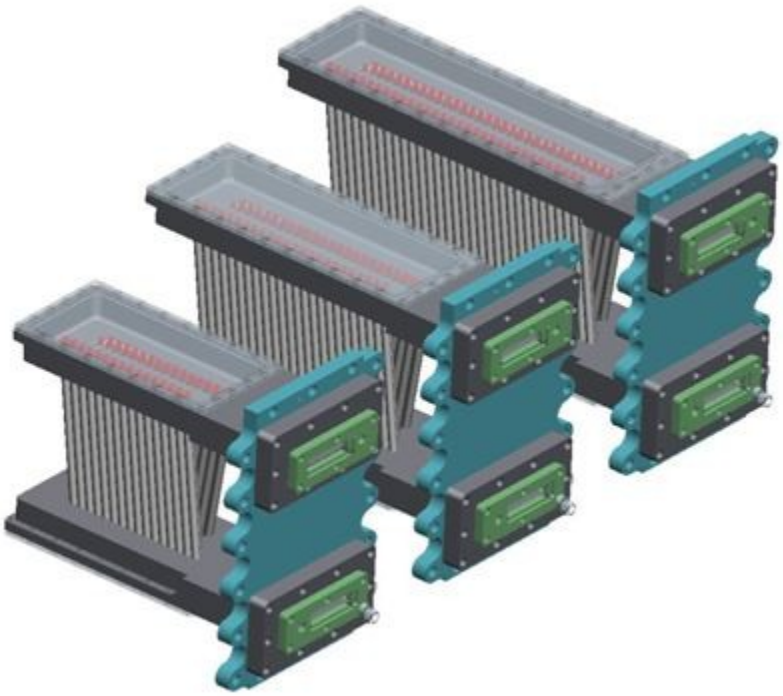

Figure 5.4: From left to right, the type-16 module, the type-24 module, and the type-32 module. (Image courtesy of John Carroll, University of Liverpool).

however, was expected to yield a higher number of good events. One way to get straws closer to the muon beam is to make all the modules longer so the straws span across the entire scallop region and vacuum chamber extension, but redesigning all the manifolds to incorporate the extra channels is impractical from both a mechanical and an electrical standpoint, given the financial budget and amount of time available. Another way to get straws closer to the muon beam is to push the modules out from the center of the storage ring and closer to the muon storage region by adding spacers to the extension arms on each module. Positioning the modules as close as possible to the trolley track is considered the ideal configuration, but a different length spacer would be necessary for each module, which increases cost and complicates the manufacture and production of the modules. Thus, four

module configurations, in addition to the Baseline configuration, were tested to determine how much the number of good events increases by moving the modules closer to the muon beam line. The results were then weighted with design and manufacturing objectives to choose a configuration for use in the E989 experiment.

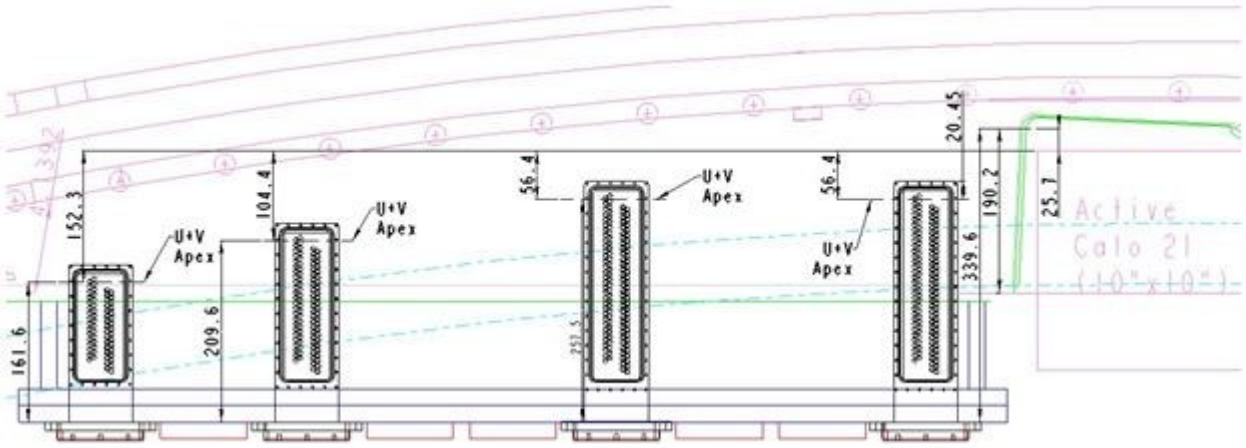

Figure 5.5: AutoCAD drawing with measurements for the three module types in the Baseline configuration. Only four of the nine modules are shown for ease in reading the measurements. (Image courtesy of Erik Voirin, FNAL).

The second module configuration used in the acceptance tests, called Placement 1, is the same as the Baseline configuration, except the modules are pushed in sets away from the center of the storage ring toward the muon storage region. Placement 1 contains four type-32 modules, three type-24 modules, and two type-16 modules. Spacers of three different lengths are needed, one for each module type.

For the third configuration, called Placement 2 and shown in Figure 5.6, the module types are switched from those in the Baseline configuration to six type-32 modules and three type-24 modules. All nine modules are positioned as close as possible to the muon storage region, without obstructing the trolley track. Placement 2 uses as many type-32 modules as

will fit in the original scallop region plus the extension to increase the total number of straws. A different length spacer is required for the extension arms on each module, but only two module types are required to be manufactured.

Similar to Placement 2, the fourth configuration, called Placement 3 and shown in Figure 5.7, contains six type-32 modules and three type-24 modules. In comparison to Placement 2, the modules for Placement 3 are pushed toward the trolley track in sets to reduce the required number of different spacer lengths from nine to four. Three different spacer lengths are needed for the type-32 modules, and one spacer length is needed for the type-24 modules.

The fifth configuration, called Placement 4, is shown in Figure 5.8. Placement 4 has one type-40 module, five type-32 modules, and three type-24 modules. The type-40 module has not yet been designed, but it is included in Placement 4 to test the effect of covering the entire front of the calorimeter with straws. Four different spacer lengths are needed, one spacer length for the type-40 module, two different spacer lengths for the type-32 modules, and one spacer length for the type-24 modules.

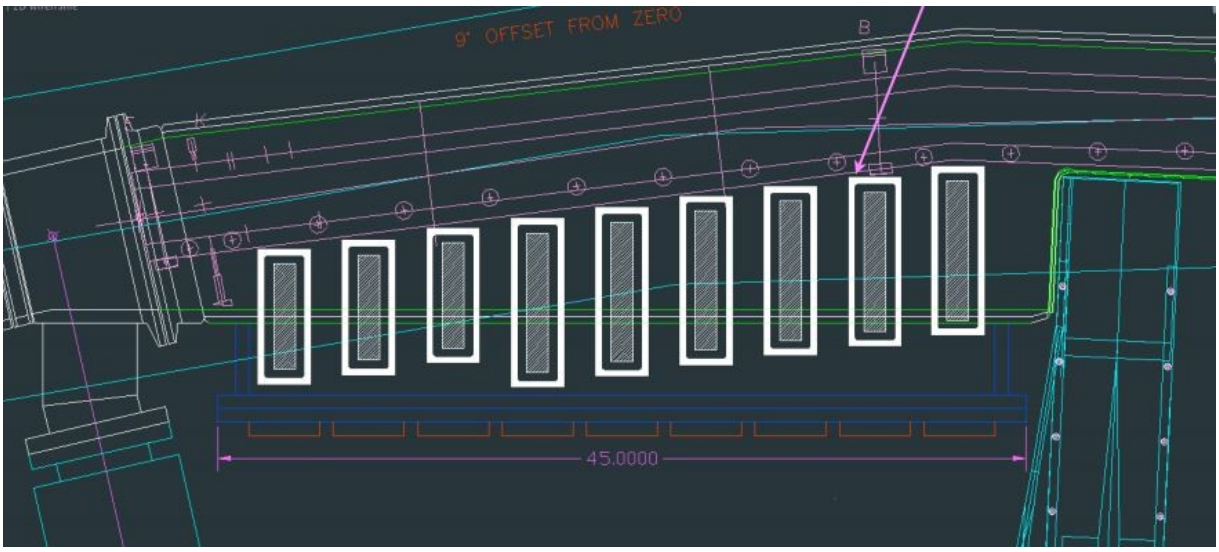

Figure 5.6: Schematic of Placement 2 for the geometry acceptance study. Placement 2 contains six type-32 modules and three type-24 modules. A different length spacer is required for each module. The purple arrow is pointing to the inside edge of the NMR trolley track. (Image courtesy of Leah Welty-Rieger, Northwestern University).

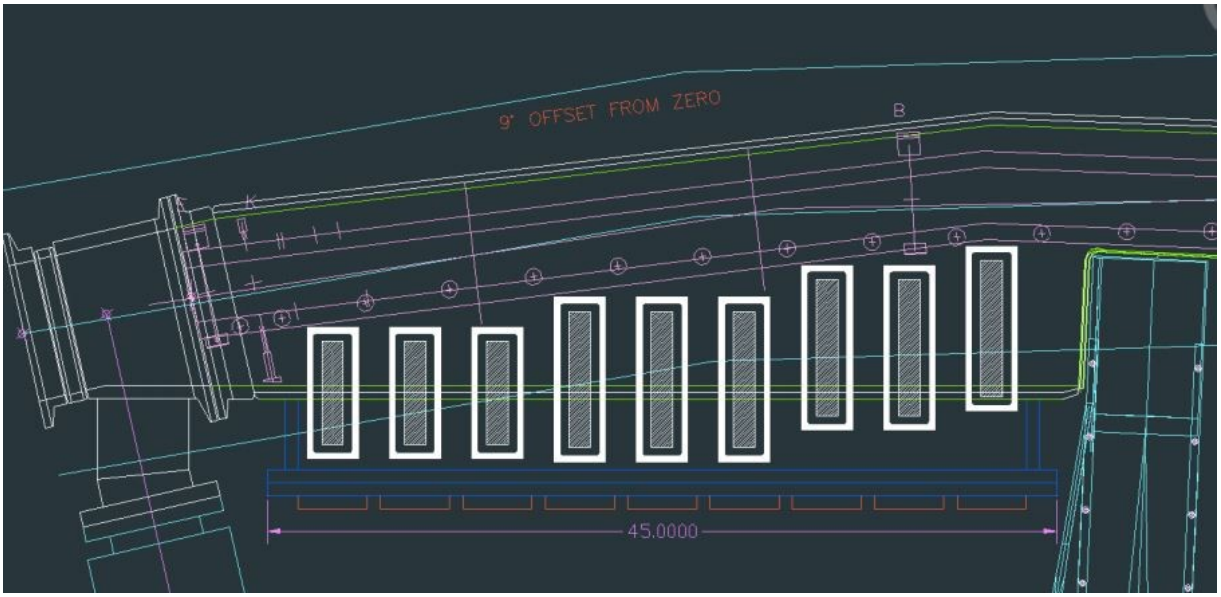

Figure 5.7: Schematic of Placement 3 for the geometry acceptance study. Placement 3 contains six type-32 modules and three type-24 modules, and four different spacer lengths are required. (Image courtesy of Leah Welty-Rieger, Northwestern University).

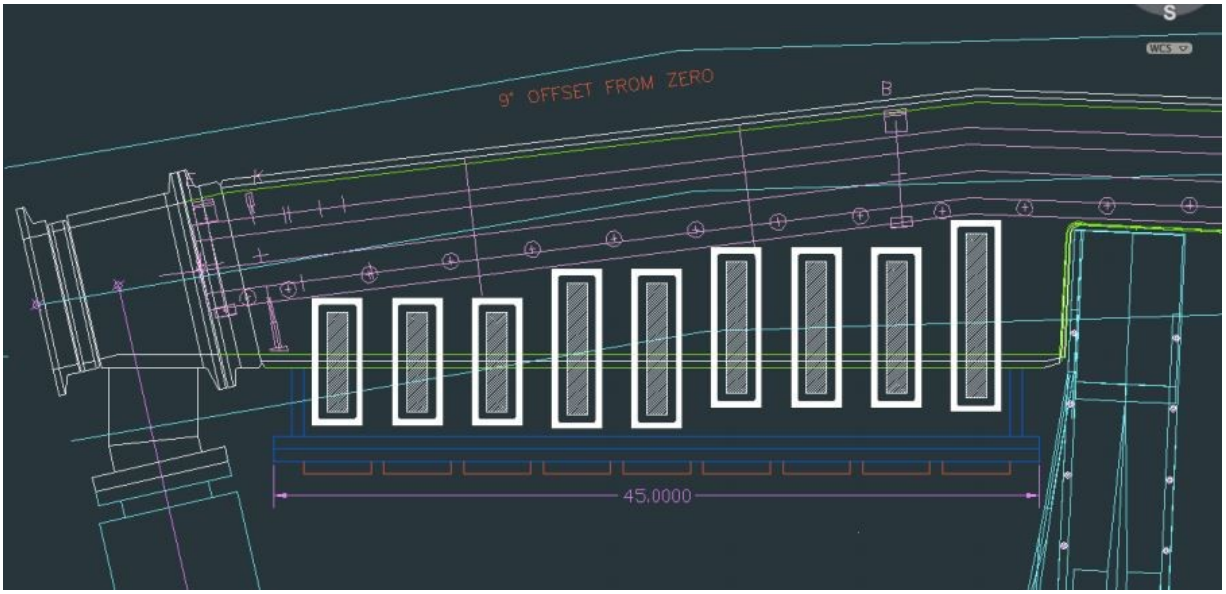

Figure 5.8: Schematic of Placement 4 for the geometry acceptance study. Placement 4 consists of one type-40 module, five type-32 modules, and three type-24 modules. The type-40 module allows the entire front face of the calorimeter to be covered with straws. Four different spacer lengths are required. (Image courtesy of Leah Welty-Rieger, Northwestern University).

For comparison, Figure 5.9 is a GEANT image showing the Baseline configuration and Placements 1-4. The NMR trolley track is not present in the GEANT visualizations, so AutoCAD drawings had to be used to determine how far out from the center of the storage ring the modules could be pushed before the modules touched the trolley track.

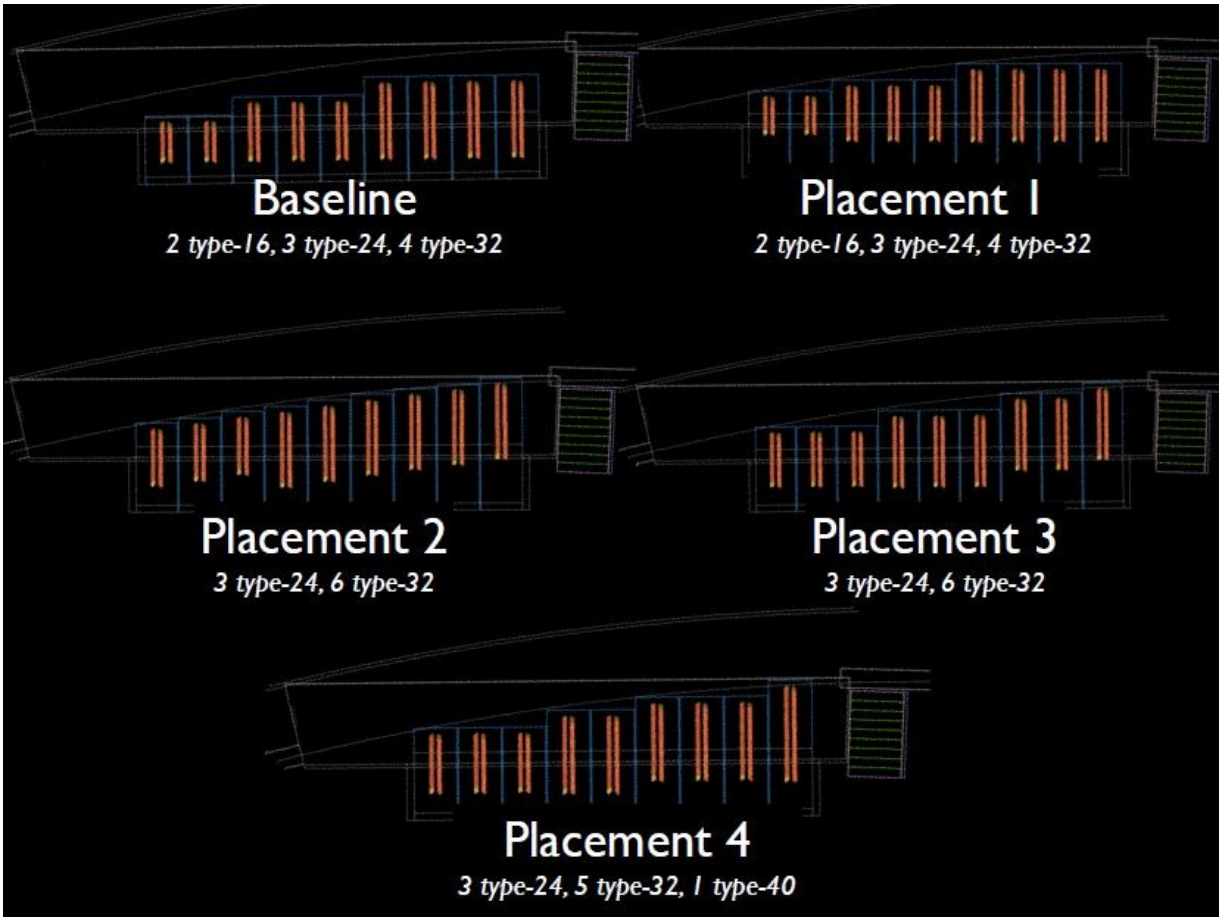

Figure 5.9: Images from GEANT showing the Baseline configuration and Placements 1-4. (Image courtesy of Leah Welty-Rieger, Northwestern University).

To begin the acceptance tests, simulation was used to generate one million events for each of the five configurations. First, a separate fcl file was written for each configuration so jobs for the five configurations could be submitted simultaneously to the Fermigrid batch system without disrupting one another. In the files, different offset values were added to the original module length to account for the various spacer lengths. Next, jobscripts were written, and the jobs were submitted. After one million events were generated for each configuration, a file list of the generated events was made for each configuration. Finally, the

parameters in the file find-and-make-golden-trackerevts.fcl were modified as needed and saved, and the file was run over each list of events. To test more than one variable, the parameters in the fcl file were changed several times, and the file rerun over all the file lists. The outputs for the runs were ROOT files. Lastly, filters and analyzers were written and run on the ROOT outputs to check the acceptance and energy distributions of the positrons.

For some of the tests, each positron was required to hit both the calorimeter and a minimum number of modules, whereas for other tests the positron was not required to hit the calorimeter. For all the tests, one event corresponded to one positron. Table 5.1 gives the number of positrons that passed out of one million total events when both the calorimeter and at least three, four, or five modules were required to be hit. When the calorimeter was not required to be hit, the results were similar, except the numbers were larger because more low energy positrons had enough energy to pass just the module requirement.

Table 5.1: The number of events passed out of one million, where each event corresponds to one positron, and the calorimeter and three to five modules were required to be hit by each positron. Results are given for the Baseline Configuration and Placements 1-4.

Number of Positrons Passed Out of One Million Total Events					
Minimum number of modules required	Baseline	Placement 1	Placement 2	Placement 3	Placement 4
3 modules + calorimeter	10, 367	19,922	23,653	26,576	18,866
4 modules + calorimeter	7,705	15,959	13,927	6,762	15,144
5 modules + calorimeter	548	3,727	7,563	5,199	5,462

The most significant results from Table 5.1 are the number of positrons that passed when the calorimeter and at least four modules were required to be hit by each positron because the current plan is to use the same requirement for the E989 experiment. As shown, the results for the Baseline configuration and Placement 3 are similar, and the results for Placements 1, 2, and 4 are similar. The Baseline configuration and Placement 3 miss about half the good events hitting both the calorimeter and at least four modules, so they are not optimal configurations. Placement 2 sees more good events and requires only two types of modules, but it needs spacers in nine different lengths, which complicates manufacturing and increases cost. Placement 4 also sees more good events and needs spacers in four, as opposed to nine, different lengths, but it requires the type-40 module to be designed and constructed, which increases cost and complicates the cooling system and the electronics inside the manifolds due to the increased channels. Placement 1 performed nearly as well as Placements 2 and 4 and requires spacers in only three lengths. Furthermore, no new modules need to be designed for Placement 1. Thus, of the configurations tested, Placement 1 is the most efficient and cost effective way to approximately double the number of good events hitting both the calorimeter and at least four modules.

When the positrons are required to hit the calorimeter and at least four modules, Placement 3 yields about the same number of good events as the Baseline configuration. Also, Placement 4 is the least feasible configuration to construct since the type-40 module would need new manifolds, electronics, and other systems to be designed. Thus, further analysis of the configurations focused on the Baseline configuration, Placement 1, and Placement 2.

Figures 5.10, 5.11, and 5.12 are plots of the wire (or straw) number versus the row number for each straw in the modules. Figure 5.10 shows the Baseline configuration, Figure 5.11 shows Placement 1, and Figure 5.12 shows Placement 2. All three figures are for the case when the positrons are required to hit the calorimeter and at least four modules to be counted as a good event. The straw rows are numbered beginning with the row furthest from the calorimeter. Each module has four rows of straws, arranged in two doublet planes, to give thirty-six rows total. The straws contain one wire each, and the wires in each row are numbered beginning with the wires closest to the center of the storage ring. The colors shown in all three plots correspond to the number of positron hits seen by the wire, and white spaces mean no positron hits were detected. Since the wires are not directly in line with each other, the "wire number" does not correspond to a spatial coordinate, so the plots do not represent a top view of the tracking stations.

Figures 5.11 and 5.12 show if the modules are moved closer to the muon beam, then a longer portion of the positron trajectory can be detected. The plots for all three configurations show if the positron is required to hit the calorimeter and at least four modules, then the largest number of positrons is detected at the fourth module from the calorimeter by the wires closest to the muon beam. Therefore, if at least four modules must be hit by the positrons, then the fourth module from the calorimeter is the most crucial module to move as close as possible to the muon beam. Figures 5.11 and 5.12 also show that positioning the first three modules from the calorimeter up against the trolley track increases the number of good events little to none, providing evidence that building a different length spacer for each module is not necessary, and the configuration in Placement 1 is sufficient to detect most of the positron

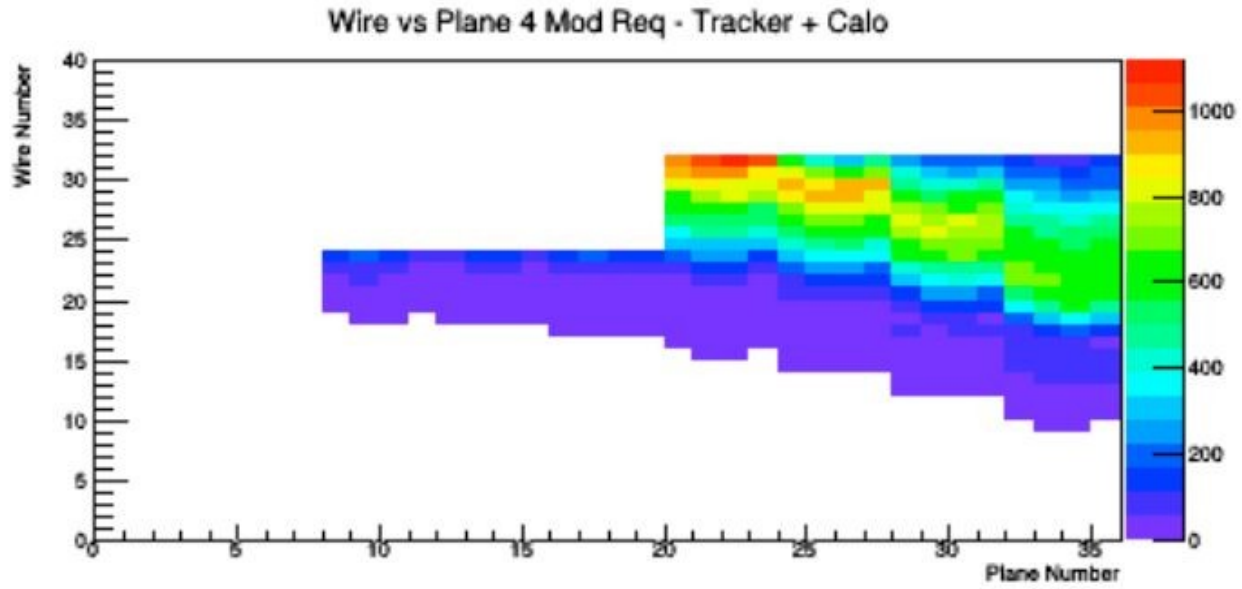

Figure 5.10: For the Baseline configuration, a plot of wire number versus row number for each straw in the modules. The positrons are required to hit the calorimeter and at least four modules to be counted as a good event. Note: "plane" number is more correctly labeled "row" number. (Image courtesy of Leah Welty-Rieger, Northwestern University).

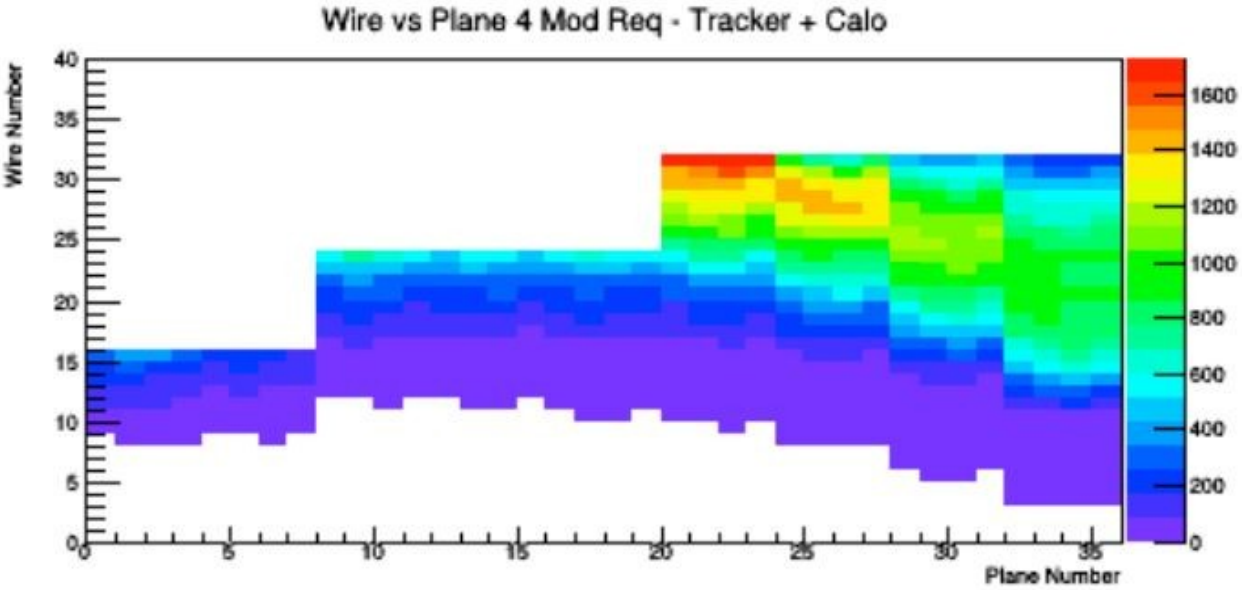

Figure 5.11: For Placement 1, a plot of wire number versus row number for each straw in the modules. The positrons are required to hit the calorimeter and at least four modules to be counted as a good event. Note: "plane" number is more correctly labeled "row" number. (Image courtesy of Leah Welty-Rieger, Northwestern University).

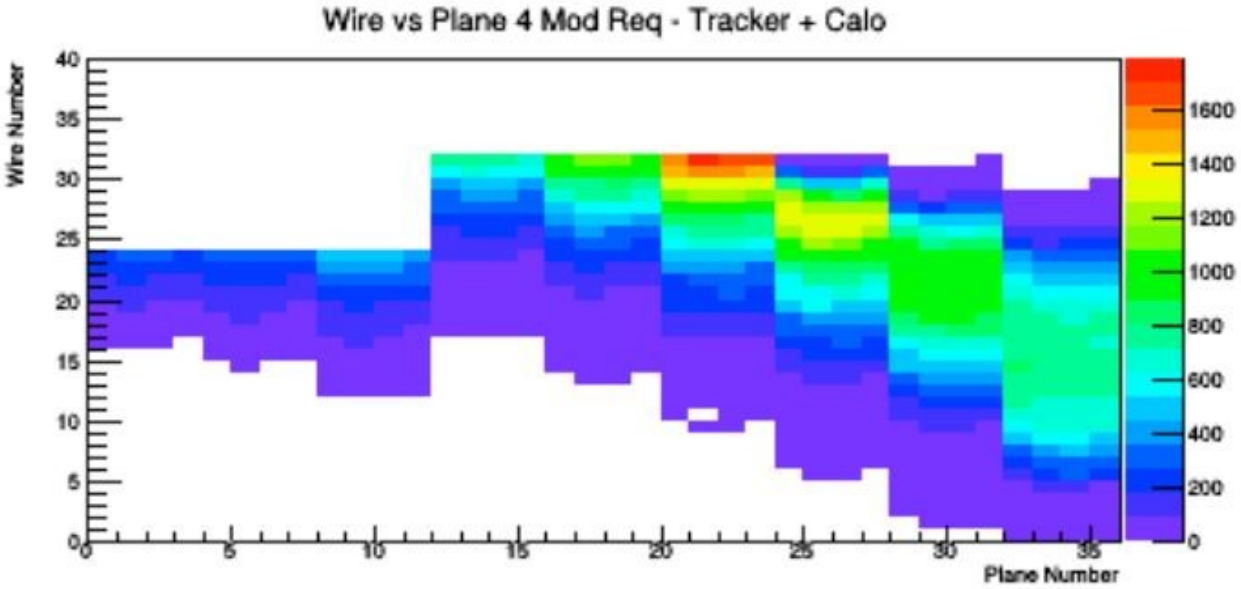

Figure 5.12: For Placement 2, a plot of wire number versus row number for each straw in the modules. The positrons are required to hit the calorimeter and at least four modules to be counted as a good event. Note: "plane" number is more correctly labeled "row" number. (Image courtesy of Leah Welty-Rieger, Northwestern University).

hits. In all three plots, the low-numbered wires closest to the center of the storage ring detect few, if any, positrons. Thus, extending the length of the manifolds to include more straws in towards the center of the storage ring would not improve the results. Also, all three plots show if the calorimeter and at least four modules are required to be hit, then the two modules furthest from the calorimeter see few to no positron hits and could potentially be eliminated, especially if the positrons are required to hit a minimum of three or fewer modules.

Figure 5.13 is a plot of wire number versus row number for Placement 1, where the positrons are required to hit at least four modules, but not the calorimeter. Comparing Figure 5.13 to Figure 5.11 shows when the calorimeter is not required to be hit, more positrons are detected by the low-numbered straws. The results make sense because if the positrons reaching the calorimeter tend to have higher energy, then removing the calorimeter

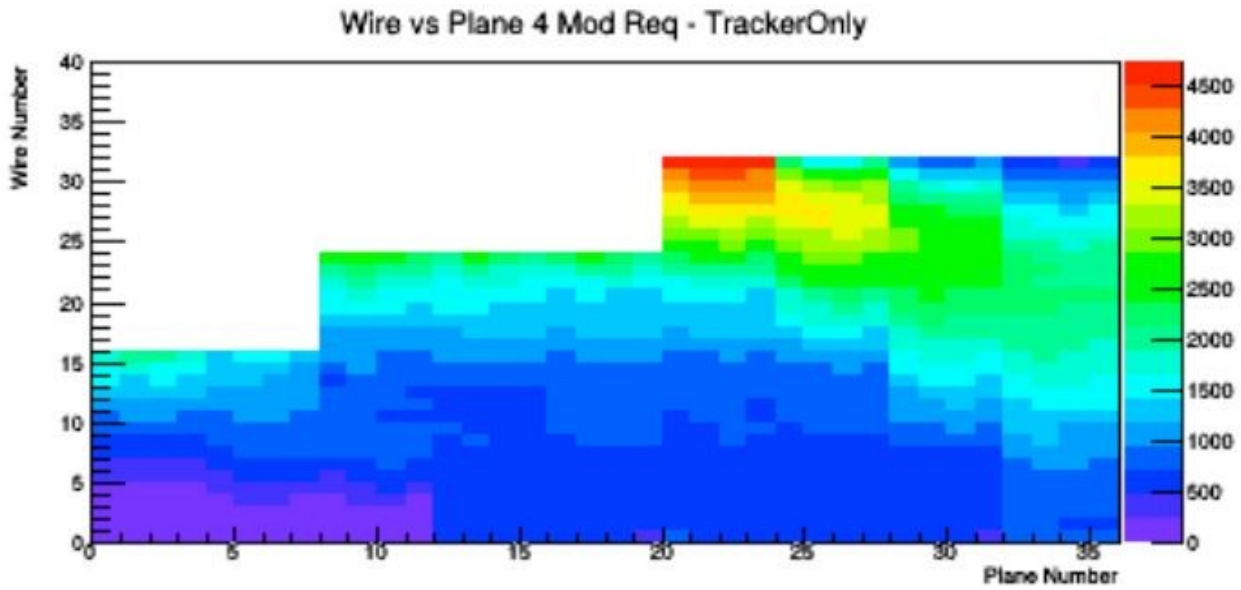

Figure 5.13: For Placement 1, a plot of wire number versus row number for each straw in the modules. The positrons are required to hit at least four modules, but not the calorimeter, to be counted as a good event. Note: "plane" number is more correctly labeled "row" number. (Image courtesy of Leah Welty-Rieger, Northwestern University).

requirement means a larger number of positrons will have sufficient energy to pass as a good event.

Figure 5.14 is a plot of wire number versus row number for Placement 1, where the positrons are required to hit the calorimeter and at least three modules to be counted as a good event. Figure 5.15 is the same as Figure 5.14, except a minimum of five models is required to be hit. In Figure 5.14, the third module from the calorimeter needs to be as close as possible to the muon beam to detect the largest number of positrons, and in Figure 5.15, the fifth module from the calorimeter becomes the most important module to move as close as possible to the muon beam. A comparison of Figures 5.11, 5.14, and 5.15 shows if a minimum of N modules is required to be hit, then the N^{th} module from the calorimeter detects the largest number of positron hits, and the hits are the most concentrated in the wires closest to the muon storage

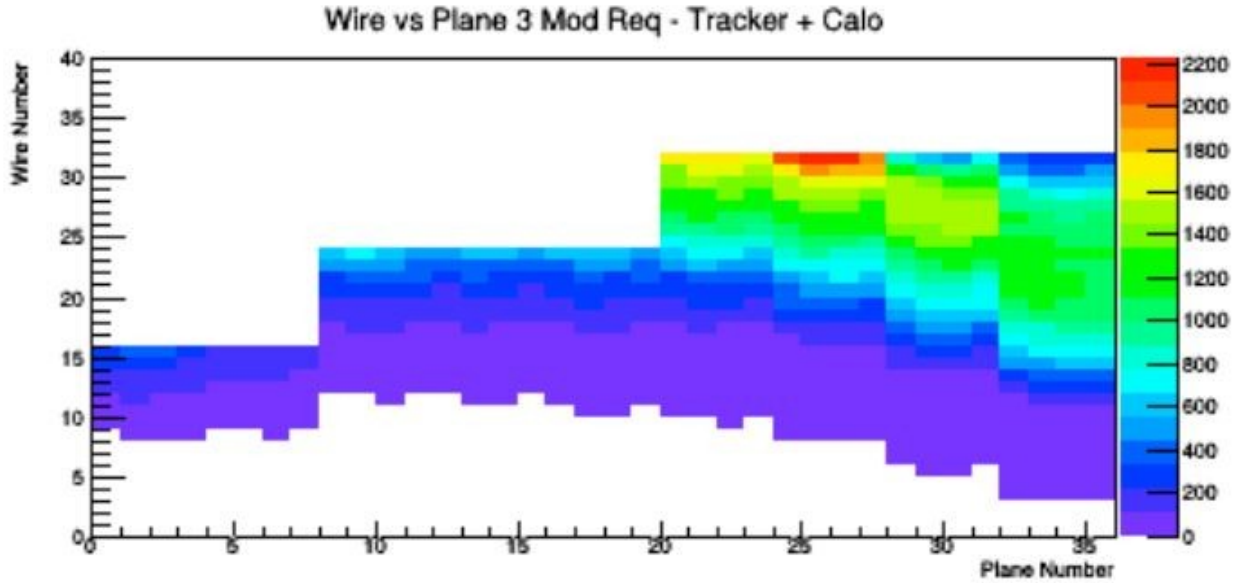

Figure 5.14: For Placement 1, a plot of wire number versus row number for each straw in the modules. The positrons are required to hit the calorimeter and at least three modules to be counted as a good event. Note: "plane" number is more correctly labeled "row" number. (Image courtesy of Leah Welty-Rieger, Northwestern University).

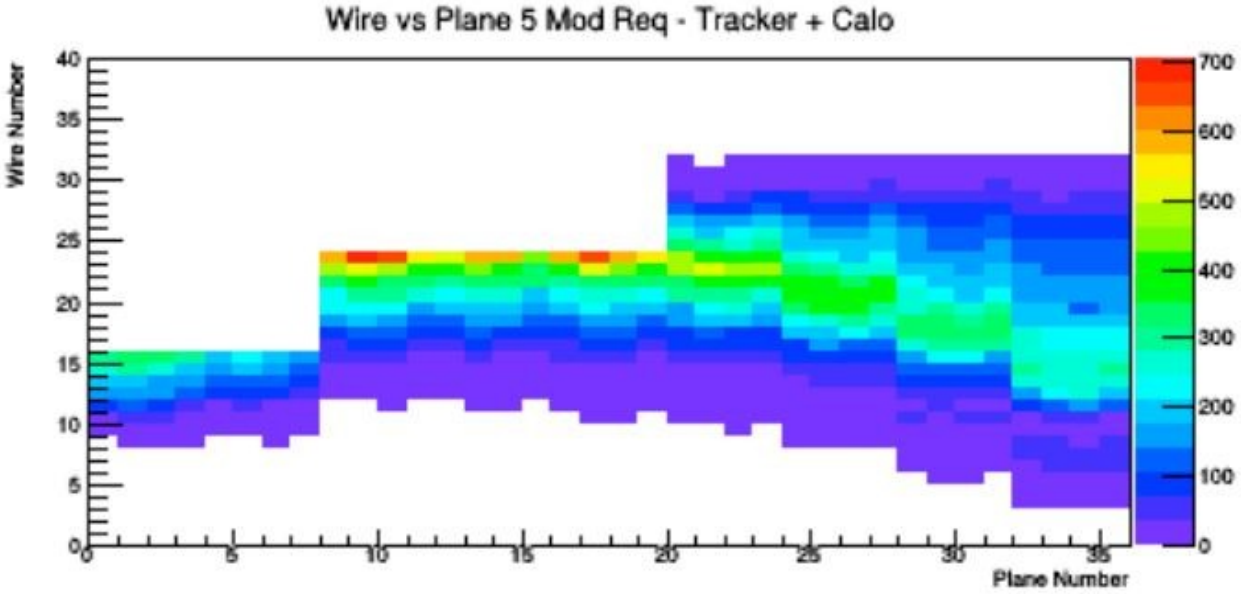

Figure 5.15: For Placement 1, a plot of wire number versus row number for each straw in the modules. The positrons are required to hit the calorimeter and at least five modules to be counted as a good event. Note: "plane" number is more correctly labeled "row" number. (Image courtesy of Leah Welty-Rieger, Northwestern University).

region. A quick look at Figure 5.7 reveals why Placement 3 detected about half as many good events as Placements 1, 2, and 4 when positron hits were required in at least four modules. In Figure 5.7, the fourth module from the calorimeter is not positioned as close as possible to the muon storage region, so many positron hits were missed.

Figure 5.16 is a plot of the number of positrons versus the positron energy in MeV measured at the calorimeter. The energy distributions of the positrons detected in the calorimeter are shown for the Baseline configuration and Placements 1 and 2. Based on the plot in Figure 5.16, the different configurations of the modules do not appear to affect the energy distribution of the positrons reaching the calorimeter.

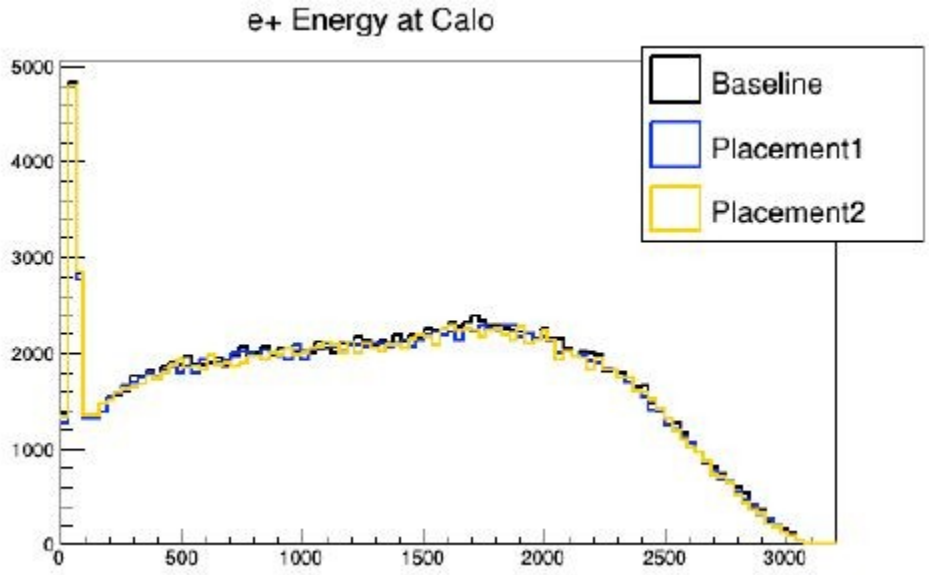

Figure 5.16: The number of positrons versus the positron energy, in MeV, measured at the calorimeter. Energy distributions for the Baseline configuration and Placements 1 and 2 are shown. (Image courtesy of Leah Welty-Rieger, Northwestern University).

Based on the results of the geometry acceptance study, Placement 1 seems to be the best module configuration to use in E989 experiment. In comparison to the Baseline configuration and Placement 3, Placement 1 approximately doubles the number of good events detected when the calorimeter and at least four modules are required to be hit by the positrons. Including a type-40 module, as in Placement 4, to cover the entire front of the calorimeter does not have a large enough effect to warrant designing a new module type with more channels. Although Placement 2 gives results similar to Placement 1, it requires spacers of a different length for each module so all the modules are positioned as close as possible to the muon beam. The results of the geometry acceptance study show, however, most of the positron hits can be detected so long as N^{th} module from the calorimeter is as close as possible to the muon storage region, and the other eight modules are reasonably close to the muon storage region. Placement 1 was chosen over Placements 2 and 4 because it requires fewer changes to the current design and is the more cost effective alternative. Thus, Placement 1 will replace the Baseline configuration for the E989 experiment.

CHAPTER 6

CONCLUSION

The New Muon g-2 E989 Collaboration at Fermilab intends to measure the muon anomalous magnetic moment a_μ to a precision of 140 ppb, which represents a four-fold improvement in the experimental precision of the current value. The E821 Collaboration at Brookhaven found the muon anomaly to differ by 3.3 to 3.6 standard deviations from the value predicted by Standard Model. The discrepancy between experiment and theory could mean the Standard Model needs to be extended to include supersymmetry, extra dimensions, the postulated dark photon, or other new forces and particles. The Brookhaven measurement, however, does not meet the 5σ discovery threshold. Thus, the E989 Collaboration will use the Fermilab accelerator complex to produce an intense muon beam so the E821 experiment can be repeated with 20 times more statistics and a maximum of 100 ppb overall statistical uncertainty. The higher precision of the E989 experiment will offer a unique way to search for new physics or, if experiment agrees with theory, the results could establish stricter limits on current and future theories. Either way, a more precise measurement of muon anomaly will help inform choices for future projects in high energy and particle physics, and provide a deeper understanding of the universe at the most fundamental level.

The muon storage ring magnet previously used at Brookhaven is central to the E989 experiment. The storage ring holds circulating muons in a uniform magnetic field of 1.451 T, constant to a few parts per million and measurable to better than one part in ten million. Due

to the high precision of the magnetic field, the storage ring was moved from Brookhaven to Fermilab to be reused. Within the storage ring, the spin angular momentum of each muon will precess about the axis of the applied magnetic field, and the muons will decay into positrons emitted preferentially along the instantaneous spin direction of the parent muon. Detectors will measure the energy and the number of high-energy positrons detected as a function of time, and the data will be analyzed to understand how much the muon's spin angular momentum is precessing. Specifically, the muon anomalous spin precession frequency ω_a and the average magnetic field $\langle B \rangle$ felt by the precession muons must be measured precisely to extract the muon anomaly at the required precession. The design, construction, shimming, and operation of the storage ring will be indispensable in obtaining the necessary measurements.

The storage ring magnet is C-shaped, and the storage region is 9 cm in diameter and located in the opening of the "C," where the magnetic field is the most uniform. The storage region will be enclosed by a set of twelve vacuum chambers, and measurements from straw tube tracking detectors and calorimeters will be used to obtain ω_a. Each vacuum chamber has two scallop regions, giving twenty-four scallop regions total, and tracking detectors will be housed in three of the scallop regions. A calorimeter will be located just outside the vacuum at the widest end of each scallop region. An indirect measurement of the muon spin will be performed by measuring the energies of the positrons produced via the weak decay of positive muons. The calorimeters will measure the energy and time of arrival of the daughter positrons. The tracking detectors will measure the muon beam profile as a function of time throughout the muon fill, verify systematic uncertainties in the measurements made by the

calorimeter, and analyze the tilt of the muon precession plane away from the vertical. Data from the tracking detectors will provide ppm level corrections to the measurement of ω_a and validify the results from the calorimeters.

Although the storage ring will be reused from the E821 experiment, the tracking detectors will be newly constructed to meet the E989 experiment's unprecedented precision goals. Due to the DC nature of the stored muon beam, the tracking detectors will contain multiple planes spread over as long a lever arm as possible. To accommodate the required number of planes with a minimum of multiple scattering, the tracking detectors will be gas based. Also, the tracking detectors will be housed within the vacuum to further minimize multiple scattering. Thus, straws will be used in the detectors because the circular geometry can maintain the differential pressure with a minimal wall thickness. Thin walls for the straws are desired to reduce the amount of material the positrons must travel through before reaching the calorimeter.

Each of the three scallop regions containing tracking detectors will have nine tracker modules. The modules will be "type-32," "type-24," or "type-16," depending on the number of straws per row. The modules will each have four rows of straws grouped together in two closely-packed doublet planes, where the planes are oriented at ±7.5° from the vertical direction. The 15° angle between the two planes in each module allows for both the vertical and horizontal position of the positron hits to be determined. The straws will be made of Mylar coated with aluminum on the outside and aluminum overlaid with gold on the inside. The active height of the straws will be 82 mm.

During assembly, the modules will undergo several quality control tests to ensure all components are working. After the modules are assembled, but before they are inserted into the vacuum chambers, the modules will also undergo a systems test using cosmic rays or a radioactive source to verify proper functioning of all channels. Results from the cosmic ray test stand experiment at NIU found if the assembled modules are tested at NIU, the lab in Faraday Hall for g-2 research is an unfavorable location to perform a systems check using cosmic rays due to the low muon count rate. Recently, however, the University of Liverpool took over the design and manufacture of the manifolds and straws, so the assembled modules will most likely be tested at Fermilab to avoid unnecessary movement of the modules.

To allow sufficient space for the completed modules to be inserted and aligned in the vacuum, an extension will be welded onto the three scallop regions that will contain modules. The vacuum extension also provides enough space in the radial direction for the module positions to be adjusted, or for the manifolds to be made longer to accommodate more straws. Tracker simulation was used to test different module types in five configurations. The configuration chosen for use in the E989 experiment, Placement 1, is similar to the current design, but with the modules pushed closer to the muon beam in groups according to module type. Simulation showed the number of good events approximately doubles when the chosen configuration is used. The results also showed the number of straws in each row of the modules does not need to be increased going in towards the center of the storage ring since the largest numbers of positrons tend to hit the wires closest to the muon beam. In an analysis of the positron energy measured at the calorimeter, different configurations of the modules did not appear to affect the energy distribution of the positrons reaching the calorimeter.

Although some of the other configurations produced results similar to the chosen configuration, Placement 1 will be used in the E989 experiment because it requires fewest changes to the current design and is the more cost effective alternative.

Design, testing, and manufacturing of the various components for the initial setup of the E989 experiment will continue until 2016 when the first beam run begins. Data analysis will occur in the coming years while the world eagerly awaits the E989 Collaboration's final announcement of a more precise value for the muon anomalous magnetic moment.

REFERENCES

Abazov, V. M., et al. (The D0 Muon Group), Nucl. Inst. Meth. **A 552**, 372-398 (2005).

Anderson, Carl D. and Seth H. Neddermeyer, Phys. Rev. **50**, 263 (1936).

Aoyama, T., M. Hayakawa, T. Kinoshita, and M. Nio, Phys. Rev. Lett. **109**, 111808 (2012).

ART homepage found at: <https://cdcvs.fnal.gov/redmine/projects/art>.

Bailey, J., et al., Nucl. Phys. **B 150**, 1 (1979).

Bennett, G. W., et al. (Muon (g-2) Collaboration) Phys. Rev. D, **73**:072003 (2006).

Beringer, J., et al. (Particle Data Group), PR D86, 010001 (2012) <http://pdg.lbl.gov/2013/reviews/rpp2013-rev-g-2-muon-anom-mag-moment.pdf>.

Carroll, John. Internal g-2 collaboration document, GM2-doc-2089-v1.

"CODATA Recommended Values of the Fundamental Physical Constants: 2010." Committee on Data for Science and Technology (CODATA). NIST.

Cox, Steve. "Introduction to μSR: What, How, Where?" ISIS Pulsed Muon Facility, Rutherford Appleton Laboratory, Chilton, Oxfordshire, OX11 0QX, UK <http://www.isis.stfc.ac.uk/groups/muons/muon-training-school/2005-introduction-cox-review7904.pdf>.

Danby, G. T., et al. Nucl. Instr. Methods. **A 457**, 151-174 (2001) <http://www.g-2.bnl.gov/publications/>.

Eisberg, Robert, and Robert Resnick. Quantum Physics of Atoms, Molecules, Nuclei, and Particles. 2nd ed. Hoboken, NJ: John Wiley and Sons, 1985.

Farley, F. J. M., Phys. Lett. **B 42**, 66 (1972).

Farley, F. J. M. and E. Picasso, in Quantum Electrodynamics, Adv. Series on Dir. In H.E.P., V7, T. Kinoshita, ed., World Scientific, 479, (1990).

Giancoli, Douglas C. Physics for Scientists and Engineers with Modern Physics. 3rd ed. Upper Saddle River, NJ: Prentice Hall, 2000.

Gnendiger, C., D. Stockinger, and H. Stockinger-Kim, Phys. Rev. **D88** , 053005 (2013).

Griffiths, David J. Introduction to Quantum Mechanics. 2nd ed. Upper Saddle River, NJ; Pearson Prentice Hall, 2004.

Harpell, Eric, Willy Langeveld, Don McShurley, Steve Shapiro, and John Venuti. "The CCRT: an inexpensive cosmic ray muon detector," SLAC-TN-95-1, Stanford Linear Accelerator Center <http://www.slac.stanford.edu/cgi-wrap/getdoc/slac-tn-95 001.pdf>.

Hutchings, Edward, Jr., ed. "Where Were the Pharaohs Buried?" Engineering and Science. **36** (6), 18 (1973) <http://calteches.library.caltech.edu/342/2/ES36.6.1973.pdf>.

Kunze, Paul, Z. Phys. **83**, 1 (1933).

Lee, S. L., R. Cywinski, and S. H. Kilcoyne, eds. Muon Science: Muons in Physics, Chemistry, and Materials. New York: Taylor and Francis Group, 1999.

Liu, W., et al., Phys. Rev. Lett. **82**, 711(1999) <http://www.bnl.gov/muong 2/papers/WL_PRL990125.pdf>.

Melissinos, Adrian C., and Jim Napolitano. Experiments in Modern Physics. Academic Press: Boston, 2003.

Mohr, P. J., B. N. Taylor, and D. B. Newell, Rev. Mod. Phys. **84**(4), 1527 (2012) <http://physics.nist.gov/cuu/pdf/RevModPhysCODATA2010.pdf>.

Neddermeyer, Seth H. and Carl D. Anderson, Phys. Rev. **51**, 844(1937).

Olive, K. A., et at. (Particle Data Group), Chin. Phys. **C38**, 090001 (2014) <http://pdg.lbl.gov>.

Roberts, B. Lee, et al. (The New Muon (g-2) E989 Collaboration), Technical Design Report, GM2 -doc-2056-v2, 2014 (unpublished) <http://gm2-docdb.fnal.gov:8080/cgi bin/ShowDocument?docid=2056>.

ROOT homepage found at: <http://root.cern.ch/drupal/>.

Schwinger, J., Phys. Rev. **76**, 790 (1949).

Stanford Scintillator Materials Group homepage found at: <http://web.stanford.edu/group/scintillators/scintillators.html>.

Welty-Rieger, Leah. Internal g-2 collaboration document, GM2-doc-2125-v1.